Cardiovascular Magnetic Resonance Imaging and MR-Conditional Cardiac Devices

24

Michael D. Eggen and Cory M. Swingen

Abstract

This chapter provides a condensed review of the basic principles of magnetic resonance imaging (MRI) and introduces the reader to some of the concepts and terminology necessary to understand the use of MRI to study the heart. We then proceed to describe a wide range of MRI cardiac applications, both in vivo and ex vivo, which should interest the biomedical engineer. While the capabilities of cardiac MRI are quite extensive, our choice of topics for this chapter is rather judicious, as cardiac MRI has evolved to the point where entire books are published on the subject.

Keywords

MRI • CMRI • Magnetic resonance imaging • Myocardial viability • Myocardial perfusion • Myocardial function • Morphology • Blood flow velocity • Fiber structure • Interventional MRI • Wall motion • Wall thickening • Myocardial strain • MR-Conditional pacemaker • MR-Conditional ICD

24.1 Introduction

"Magnetic resonance imaging" (MRI) of the heart has rapidly become very popular worldwide, because of its clinical versatility and flexibility, i.e., since it allows one to acquire information on anatomical structure and function simultaneously. An additional benefit of MRI is that patients are not subjected to any ionizing radiation or invasive procedures (e.g., catheterization). Recently, many specialized MR techniques have become available for cardiovascular imaging and thus may potentially replace other types of imaging modalities. As such, cardiac MR may become the "one-stop shop" for imaging, as it is able to: (1) measure myocardial blood flow; (2) differentiate viable from nonviable myocardial tissue; (3) depict the structure of peripheral and coronary vessels (magnetic resonance angiography); (4) measure blood flow velocities (MR velocity mapping); (5) examine metabolic energetics (MR spectroscopy); (6) assess myocardial contractile properties (multislice, multiphase cine imaging, MR tagging); and/or (7) guide interventional procedures with real-time imaging (interventional MRI). The capabilities of MRI as a tomographic imaging modality to capture, with high spatial resolution, the anatomy of 3D structures were already well appreciated before the first attempts were made to apply MRI to the heart. Yet cardiac motion, compounded by respiratory motion and turbulent blood flow in the ventricular cavities and large vessels, initially imposed formidable barriers to the acquisition of artifact-free images that could depict cardiac anatomy with sufficient detail. It has taken well over a decade for cardiac MRI to mature to the point where it is currently being applied in routine fashion in the clinical setting. Therefore, in future medical centers of

---

Electronic supplementary material: The online version of this chapter (doi:10.1007/978-3-319-19464-6_24) contains supplementary material, which is available to authorized users. Videos can also be accessed at http://link.springer.com/book/10.1007/978-3-319-19464-6_24.

M.D. Eggen, PhD (✉)
Medtronic, 8200 Coral Sea Street NE, Mounds View,
Minneapolis, MN 55112, USA
e-mail: michael.d.eggen@medtronic.com

C.M. Swingen, PhD
Department of Medicine, University of Minnesota,
Minneapolis, MN, USA

P.A. Iaizzo (ed.), *Handbook of Cardiac Anatomy, Physiology, and Devices*, DOI 10.1007/978-3-319-19464-6_24

excellence, other cardiac imaging modalities such as ultrasound imaging and nuclear imaging may be partially eclipsed by MRI for selected applications.

This chapter provides a condensed review of the basic principles of MRI and introduces the reader to some of the concepts and terminology necessary to understand the application of MRI to the heart. We then proceed to describe a wide range of cardiac applications of MRI, both in vivo and ex vivo, which should interest the biomedical engineer. While the capabilities of cardiac MRI are quite extensive, our choice of topics for this chapter is rather judicious, as cardiac MRI has evolved to the point where entire books are published on the subject.

24.2 Overview of MRI

MRI works using the principle of nuclear magnetic resonance. That is, in the presence of a strong magnetic field (typically 1.5–3 Tesla range for clinical systems), protons in the body are stimulated to emit radio waves. These radio waves are detected by an antenna, or coil, placed around the body region of interest and the signals are decomposed to reconstruct an image. We present a short summary of the basic concepts here and refer the reader to the overall literature for an in-depth examination.

24.2.1 Resonance

Inside the MRI scanner protons in the body align with the magnetic fields, similar to what happens to a compass needle placed in a magnetic field. These magnetic dipoles, if tipped away from the direction of the magnetic field, will precess about the direction of the static magnetic field (Fig. 24.1). This precession has a rotation frequency, ν_L, that is directly proportional to the magnetic field strength B_0. For hydrogen nuclei, the precession frequency varies with field strength as:

$$\nu_L = 42.6(\mathrm{MHz/Tesla}) \cdot B_0(\mathrm{Tesla}).$$

The precession frequency is also known as the *Larmor frequency*. Tipping a nuclear magnetic moment away from the direction of the z axis (B_0 direction) can be accomplished by applying an oscillating magnetic field, denoted by B_1, in a direction perpendicular to B_0. The radiofrequency transmitter should be tuned to a frequency close to the Larmor frequency to elicit a resonant excitation. After a radiofrequency excitation pulse, the static magnetic field, B_0, causes precession of the transverse magnetization component, which can be detected with an external coil as shown in Fig. 24.2. It is customary to refer to the magnetic fields which are oscillating at radiofrequencies and turned on for brief durations as *radiofrequency pulses*. A pulse that tips the magnetic moment from the z axis into the x–y plane is referred to as a *90° radiofrequency pulse*; a pulse that inverts the orientation of the magnetic moment is called a *180° or inversion pulse*. In general, the degree to which the spins are tipped into the transverse (x–y) plane is referred to the *flip angle*.

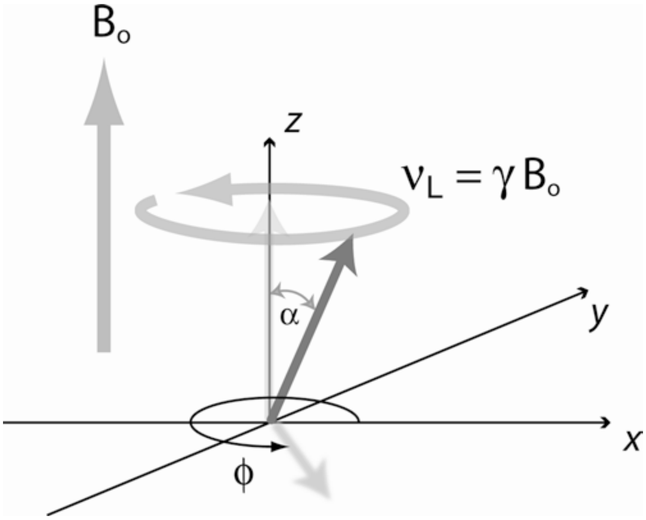

Fig. 24.1 A single magnetic dipole moment in a static magnetic field of strength, B_0. It is customary to align the z axis of a rectangular coordinate system with the direction of the externally applied static magnetic field, B_0. In this example, the magnetic moment, initially aligned with the applied magnetic field, was tipped away from the z direction by an angle α through application of an oscillating magnetic field (not shown). The oscillating magnetic field is kept on only for the time necessary to tip the magnetic dipole moment by a certain angle, α in this example. After turning the oscillating magnetic field off, the magnetic dipole moment precesses about the B_0 direction at a frequency, $\nu_L = \gamma B_0$, where γ is a constant, the gyromagnetic ratio, and represents a property of the nucleus. For ^{1}H nuclei, γ equals 42.6 MHz/Tesla. The angle ϕ denotes the phase angle of the magnetization component in the x–y plane, orthogonal to the direction of B_0

Immediately after a radiofrequency excitation, individual magnetic moments that were tipped into the transverse plane become in-phase, i.e., they have the same phase angle. If all magnetic moments were to precess at exactly the same Larmor frequency, this phase coherence would persist. Residual magnetic field inhomogeneities, magnetic dipole interactions between neighboring nuclei, molecule-specific shifts of the precession frequency, and other factors produce a distribution of Larmor frequencies. The frequency shifts relative to a reference frequency can be tissue-specific, as in the case of ^{1}H nuclei in fatty tissue. The spread of Larmor frequencies results in a slow loss of phase coherence of the transverse magnetization, i.e., the sum of all transverse magnetization components decays with time. The decay following a radiofrequency excitation is called *free induction decay*, and often has the shape of an exponential function with an exponential time constant denoted as T_2, roughly on the order of ~0.1 to ~10^2 ms for ^{1}H nuclei in biological systems. In the presence of field inhomogeneities and other

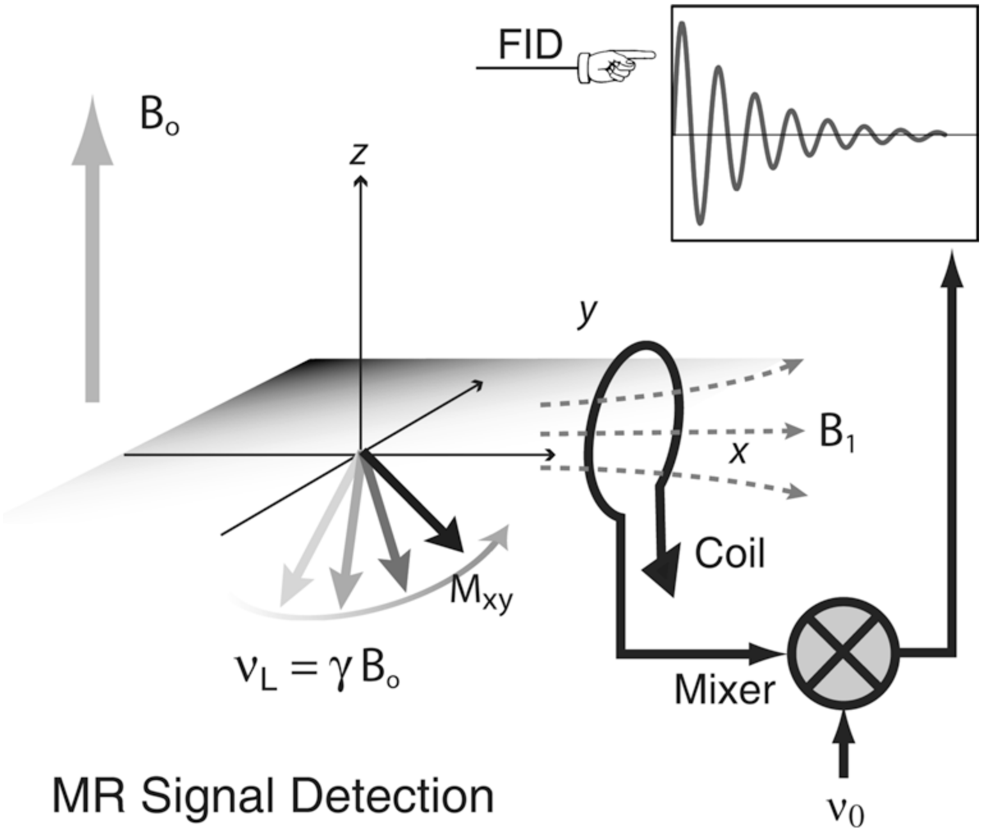

Fig. 24.2 The transverse magnetization component of a nuclear dipole precesses at the Larmor frequency, and produces an oscillating magnetic flux density that can be detected with a wire loop that is part of a resonant circuit. The induced voltage is amplified and mixed with the signal of an oscillator. The low frequency component from the mixer is a free induction decay with frequency, $\nu_L - \nu_o$. Often two coils, oriented perpendicular to each other, are used to detect the signal from the *Mx* and *My* components of the transverse magnetization, which are in quadrature, i.e., they have a relative phase difference of 90°. By detection of the quadrature components, it is possible to determine the sign of the difference $\nu_L - \nu_o$, and by combination of the two signals, after phase shifting one by 90°, one improves the signal-to-noise by a factor of $\sqrt{2}$. *FID* free induction decay, *MR* magnetic resonance

factors that cause a spread of Larmor frequencies, the transverse magnetization decay is further shortened. To distinguish this latter situation, one introduces a time constant, T_2^*, that is characteristic of the exponential decay of the transverse magnetization in "heterogenous" environments. It follows that T_2^* is always shorter than T_2.

After any radiofrequency excitation that tips the magnetization vectors away from the direction of the applied static magnetic field, B_0, the nuclear spins will, over time, realign themselves with the magnetic field to reach the same alignment as before the radiofrequency excitation. This time constant is denoted as T_1.

24.2.2 The Echo

A loss of phase coherence due to any spread in Larmor frequencies, for example, due to magnetic field inhomogeneities, can be (at least partially) reversed by applying a 180° pulse that flips the magnetization in the *x*–*y* plane such that the faster precessing spins now lag behind and the more slowly precessing spins are ahead, compared to spins precessing at the mean Larmor frequency. Once the echo amplitude peaks, the spread of Larmor frequencies again causes a loss of phase coherence. Multiple 180° pulses can be applied to repeatedly reverse the loss of phase coherence and thereby produce a train of spin echoes, referred to as *fast spin echo imaging*. The decay of the spin echo amplitudes is governed by the decay constant T_2, while a free induction decays with a characteristic time constant T_2^*, with $T_2^* < T_2$. Importantly, for cardiac imaging applications, it is useful to note that the spin echo (and spin echo trains in particular) provides a method to attenuate the signal from flowing blood, while obtaining "normal" spin echoes from stationary or slow moving tissue.

Spin echoes provide an effective means of refocusing the transverse magnetization for optimal MR signal detection. A similar, but nevertheless different, type of echo-like effect can be achieved by applying two magnetic field gradient pulses of opposite polarity instead of a 180° radiofrequency pulse. The first gradient pulse causes a rapid dephasing of the transverse magnetization; the second gradient pulse, of opposite polarity, can reverse this effect. An echo-type signal is observed, and peaks at the point where the phase wrap produced by the first pulse is . This type of echo is called a *gradient echo*.

A train of gradient echoes can be created by consecutive pairs of dephasing and rephasing gradient waveforms. The acquisition of multiple phase-encoded gradient echoes after a single radiofrequency excitation is useful for very rapid image acquisition, but is limited by the T_2^* decay of the signal.

A variation of the gradient echo technique that reestablishes phase coherence to the best possible degree before application of the next radiofrequency excitation (i.e., the next phase encoding step) can be used to produce a steady state. This allows the application of radiofrequency pulses with fairly large flip angles. Instead of relying on T_1 relaxation to return the magnetization from the transverse plane to the B_0 direction, the magnetization is toggled back and forth by the radiofrequency pulses between the z axis and the transverse plane. The attainable signal-to-noise ratio with this approach is significantly higher than with "conventional" gradient echo imaging. This type of gradient echo imaging is referred to in the literature by various acronyms—*steady-state free precession imaging*, *true FISP*, or *balanced fast field echo imaging*. In particular, for cardiac cine studies, this technique has led to a marked improvement of image quality. Steady-state free precession (SSFP) works best with very short repetition times which, in turn, impose high demands on the gradient system of the MR scanner in terms of ramping gradients up and down.

24.2.3 Image Contrast

Biological tissues and blood have approximately the same density of ^{1}H nuclei, and spin-density images show poor contrast to differentiate (e.g., tissue from blood or fat from muscle). One of the most appealing aspects of MRI is the ability to manipulate the image contrast, based on differences in the T_1 or T_2 relaxation times. For a gradient echo sequence, the T_1 weighting is determined by the combination of flip angle and repetition time. Reducing repetition time or increasing the flip angle increases the T_1 weighting in the image.

The T_2^* weighting of a gradient echo image is controlled by the time delay between the radiofrequency pulse and the center of the readout window, i.e., the echo time TE. The T_2 weighting the spin echo signal is similarly determined by the echo time. In a fast spin echo sequence, one can use multiple echoes to read out the signal with different phase encodings for each echo. Controlling the T_1 weighting through adjustment of repetition time and the flip angle imposes some limits that can be circumvented by applying an inversion pulse before the image acquisition and performing the image acquisition as rapidly as possible. The time between the inversion pulse and the start of the image acquisition controls the T_1 contrast in this case. The image acquisition after the magnetization inversion is typically performed with a gradient echo sequence that uses small flip angles, i.e., the T_1 contrast is controlled by the prepulse and the delay after the prepulse, instead of the repetition time and the flip angle, α, of the gradient echo image acquisition. Gradient echo imaging with a magnetization preparation in the form of a 180° or 90° radiofrequency pulse is often the method of choice to acquire rapidly T_1-weighted images of the heart.

MR contrast agents, such as gadolinium, provide a further means for controlling the image contrast by injecting a compound with paramagnetic ions that reduce the T_1 of blood and tissue permeated by the agent. The local T_1 reduction depends on: (1) delivery of contrast agent to the tissue region through the blood vessels; (2) the degree to which the contrast agent molecules can cross barriers such as the capillary barrier; and (3) the distribution volume of the contrast agent within the tissue. The contrast seen after the injection of such an agent can be used to determine pathology, such as the breakdown of the cardiac cell membranes and/or an above normal concentration of contrast agent in infarcted myocardium.

24.3 Cardiac MR Techniques and Applications

24.3.1 Cardiac Morphology

The accurate depiction of cardiac morphology is important in most imaging applications. Numerous MR techniques have been developed and they are generally categorized based on the appearance of the intracardiac blood in the image, as either *black-blood* or *bright-blood* techniques.

Spin-echo (SE) was the first sequence used for the evaluation of cardiac morphology, however it was not until the advent of ECG-gating that SE imaging became substantially more important by reducing motion artifacts associated with the beating heart. SE images are called *black-blood* images due to the signal void created by flowing blood, which provides very good contrast between the myocardium and the blood. Slower moving blood, particularly adjacent to the ventricular walls, however, can cause the blood signal to appear brighter, effectively reducing the quality of the image. So, presaturating with a radiofrequency pulse and reducing the echo time (TE) is used to minimize the blood signal and increase the contrast in the image [1]. Although widely available, SE imaging is limited due to its poor temporal resolution and susceptibility to respiratory and other motion artifacts. Nevertheless, these problems have been overcome through the development of sequences with shorter acquisition times, so-called fast (or turbo) SE pulse sequences. Although soft tissue contrast is not as optimal, these sequences have become the frontline sequence for depiction of cardiac morphology (Fig. 24.3).

24.3.2 Global Cardiac Function

Global and regional assessments of ventricular function with MRI are very well established and have been shown to be accurate and reproducible compared with other imaging modalities for the calculation of volume, mass, and derived

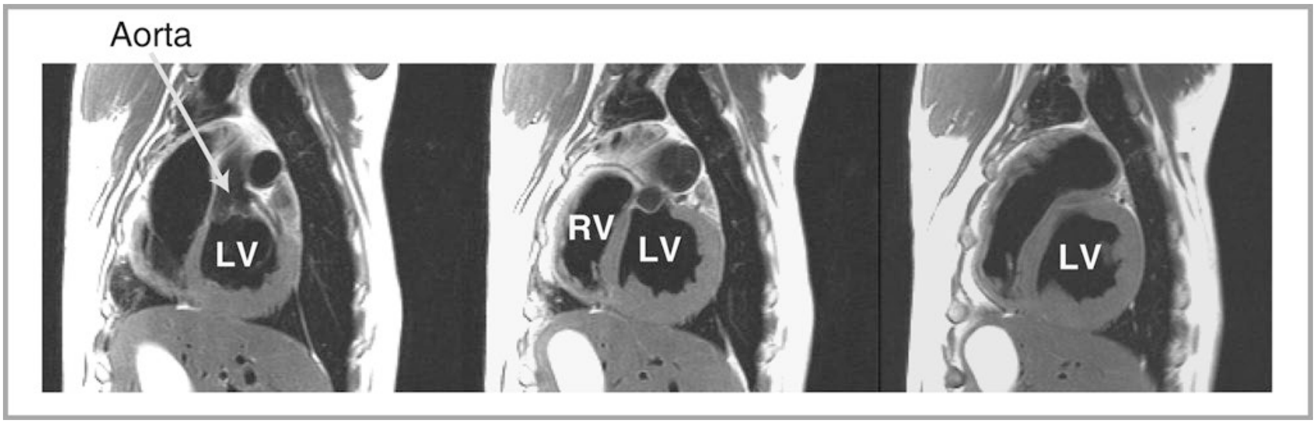

Fig. 24.3 Cardiac anatomy of a canine heart imaged with a *T2-weighted* fast spin echo sequence and in-plane resolution of 1.2 mm. Cardiac structures such as the left ventricle (*LV*), right ventricle (*RV*), and aorta are labeled. The signal from blood in the ventricular cavities was nulled by a magnetization preparation consisting of radiofrequency inversion pulses. Furthermore, the use of an echo train (with seven spin echoes in this case) and a long effective echo time also causes attenuation of the signal from moving blood. These so-called *black-blood* imaging techniques are very useful for anatomical imaging to avoid image artifacts from flowing blood

parameters such as stroke volume and ejection fraction [2, 3]. Thus, it is now considered the gold standard for the evaluation of cardiac function and mass in numerous studies comparing different imaging modalities [4].

Cine loops are acquired to follow the changes in ventricular dimensions over the entire cardiac cycle and thus to assess cardiac function. The acquisition of each image in the cine loop is broken up into several "segments," and the image segments are acquired over consecutive heart beats, as shown in Fig. 24.4. The acquisition of such image segments for each cardiac phase is subsequently synchronized with the heart cycle by gating of the encoding steps with the patient's electrocardiogram. This technique works well as long as the subject has a regular heart beat. The final result of the segmented acquisition is a series of images, one for each phase of the cardiac cycle. These images can be played as a cine loop, e.g., to assess ventricular function. To increase the sharpness of the quality of images, clinicians ask patients to hold their breath during image acquisition. The segmented data acquisition approach always involves a tradeoff between temporal resolution (i.e., number of frames covering one R-to-R interval) and spatial resolution, as the image acquisition needs to be performed within a time short enough to allow for suspended breathing.

Typically, for the measurement of global cardiac function, *bright-blood cine MRI* is performed in multiple short-axis views, covering the heart from base to apex, using a multiphase, segmented *k*-space, *gradient echo* (GRE) sequence [5–7]. Yet to date, GRE studies have suffered due to saturation effects in areas of low blood velocity, causing reduced contrast between blood and myocardium within the ventricular cavity [8]. In general, this problem causes difficulties in detection of the endocardial border, most dramatically in long-axis views of the heart where there is very minimal motion of blood through the imaging plane, as the majority of blood is moving within the image plane in these views as shown in Fig. 24.5A. Such problems associated with GRE cine imaging have recently been minimized with the advent of SSFP sequences (Fig. 24.5).

Although the concept of SSFP imaging has been described in the literature for many years, only recently has MR hardware developed to the point that these techniques have become practical and available on clinical scanners (e.g., those from multiple vendors) [9, 10]. SSFP sequences have dramatically improved contrast-to-noise, shortened acquisition times, and increased both spatial and temporal resolution in comparison with previous GRE techniques [2, 11, 12]. These improvements have enhanced the detection of the epicardial and endocardial surfaces (delineation of trabeculation and papillary muscle), both manually and with automated detection schemes, resulting in improved accuracy and reproducibility for the quantification of cardiac mass and volumes [13, 14]. Scan times have been reduced as well, such that SSFP sequences for an entire 3D data set covering the heart can be acquired within a single breath-hold.

SSFP techniques are also employed in the emerging area of real-time MR imaging. Recently, real-time imaging techniques have been developed and improved such that they will be employed in future cardiac function studies, as well as in the emerging field of interventional imaging with MRI. These real-time sequences continuously acquire images of the heart with sufficiently high temporal resolution similar to fluoroscopy [15] without the need for ECG triggering or breath-holding, therefore making it possible to image patients with severe arrhythmias or heart disease. In the past, these were difficult requirements to fulfill with segmented *k*-space GRE or SSFP sequences. Furthermore, newly developed sequences implementing image reconstruction techniques with sensitivity encoding (SENSE) and simultaneous acquisition of spatial harmonics (SMASH) have reported imaging temporal resolutions down to 13 ms with a spatial resolution of 4.1 mm [16].

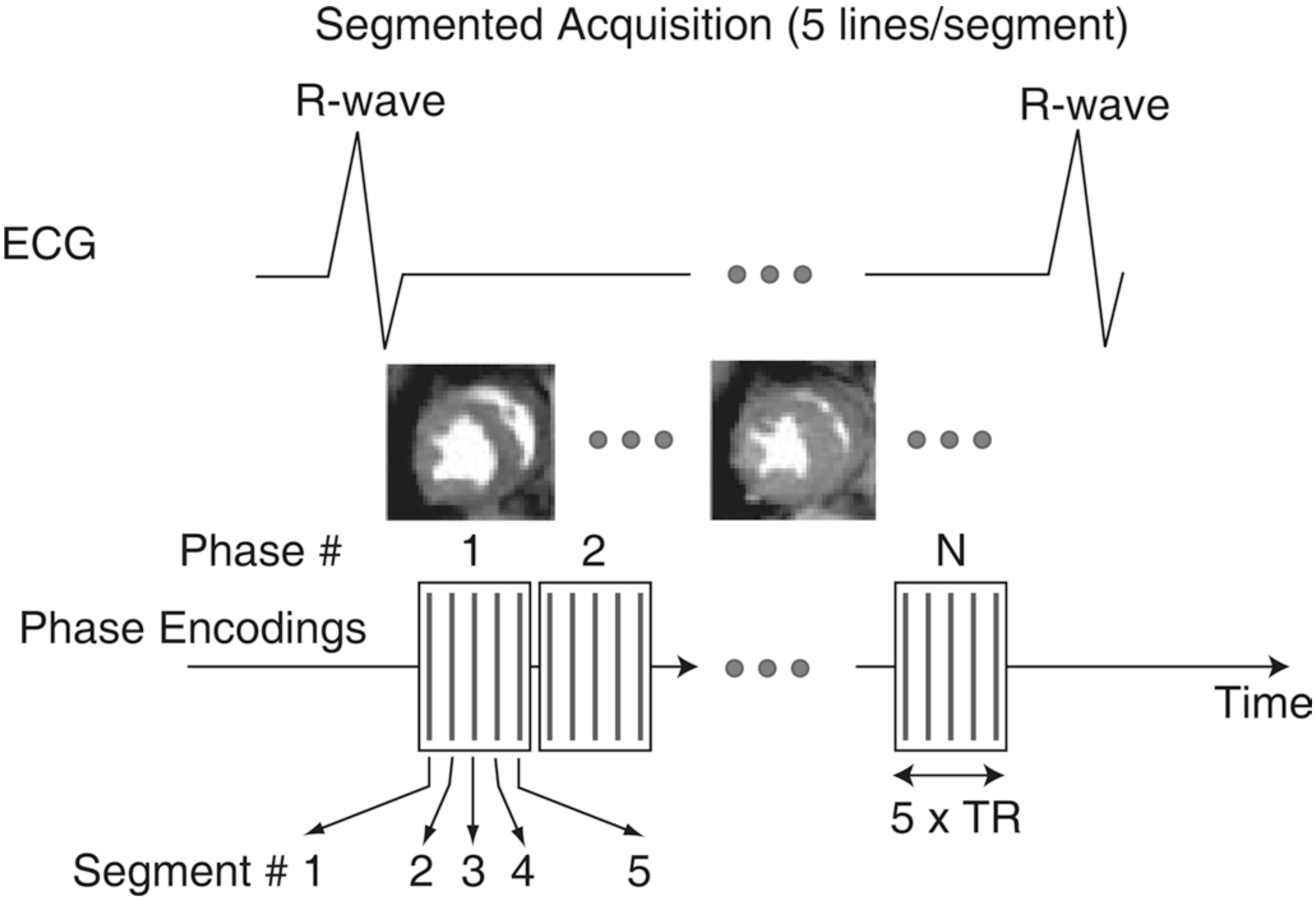

Fig. 24.4 Illustration of the principle of segmented acquisition of data, as that used for imaging multiple phases of the cardiac cycle in ventricular function studies. The image acquisition is synchronized to the cardiac cycle by triggering of the pulse sequence with the R-wave on the ECG. The total number of phase encodings is split into five groups or segments in this example. The same five phase encodings are performed during each phase of one cardiac cycle. During the next R-to-R interval, five other phase encodings are performed for each cardiac phase. The R-wave-triggered acquisition of phase encodings is repeated k number of times to obtain a total of $k \cdot 5$ phase encodings. The temporal extent of each cardiac phase is shown in the diagram by the *boxes* that contain the symbolic representations of the phase-encoded lines as *vertical lines*. The temporal resolution (TR) of the resulting cine loop is determined by the number of lines per segment (five in this example) and the repetition time for each phase encoding step. Typical resolutions are on the order of 40–50 ms for resting heart rates, and higher during inotropic stimulation of the patient's heart. The image acquisition is performed while the patient holds his/her breath. In this example the required duration of the breath-hold would be k heart beats, with k typically on the order of 10–20, depending on the heart rate

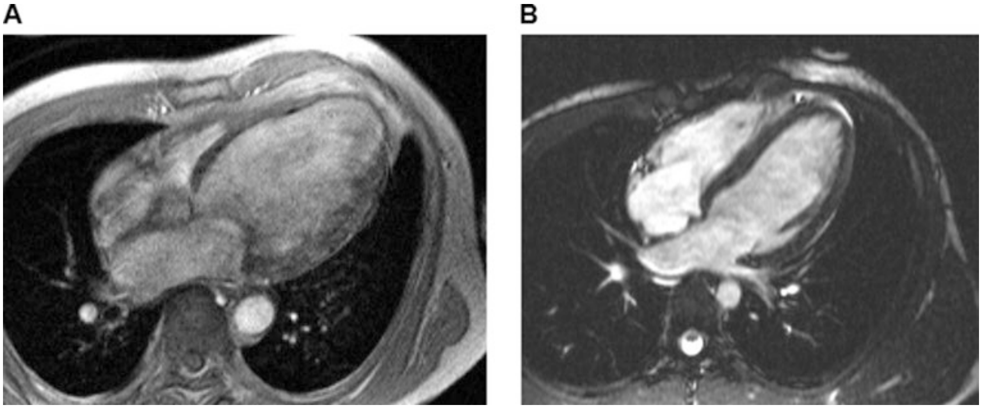

Fig. 24.5 Comparison of end-diastolic long-axis views acquired with a segmented gradient echo sequence (*left*) and a steady-state free precession (*SSFP*) sequence (*right*). The SSFP technique provides significantly higher contrast to noise between intraventricular blood and myocardium, resulting in improved endocardial border definition throughout the cardiac cycle, as compared with the older gradient echo sequence

24.3.3 Regional Myocardial Function

Ventricular volumes and derived parameters such as stroke volume and ejection fraction are the most commonly used variables for the assessment of systolic function in the clinical setting, however they have associated limitations related to the measurement of contractile properties of the heart. Furthermore, these descriptors of cardiac performance do not take into consideration the importance of regional contractile dysfunction, the degree and extent of which are important prognostic factors with ischemic heart disease, and/or following myocardial infarction [17–19]. It is generally accepted that quantitative estimates of wall motion and relative changes in wall thickening (expressed as % of end-diastolic wall thickness) are useful for measuring regional function and are also more precise than the subjective visual wall motion scoring system which is commonly used in the clinic today [20, 21]. Wall motion changes and thickening are usually measured along the length of a center line between the segmented endocardial and epicardial borders of the heart. They are further divided into myocardial segments of equal circumferential extent which are positioned relative to the location of an anatomical landmark such as the anterior-septal junction of the left ventricle and right ventricle. Dynamic changes in wall thickening can be considered as the radial component of myocardial strain, defined as the percent change in dimension from a resting state. Such strain analyses have proven very useful for the assessment of regional contractile function in both animals and human patients [22–24].

Circumferential shortening and radial thickening are two components of myocardial strain typically assessed by MRI tagging [25–29]. This approach has a higher sensitivity to the identification of noncontracting regions of the myocardium compared to "conventional" cine MRI. As such, cine imaging of the heart can be combined with a series of magnetization preparation pulses that null the longitudinal magnetization along thin parallel stripes in the slice plane. The stripes or tags appear as black lines on the MR images and can be applied in two directions in a single slice, forming a grid pattern. This grid pattern is created immediately after the R-wave of the EKG and before acquisition of the segmented phase encodings (Fig. 24.4). The grid tags visible in the resulting images are "imbedded" in the tissue and are therefore distorted if any myocardial motion occurs. Thus, intramyocardial displacements and myocardial strain can be tracked through monitoring visible motion and deformation of the tag lines, respectively. Figure 24.6 shows an example of a myocardial grid pattern laid down at end-diastole and, in a second frame, the same pattern is recorded at end-systole with evident distortion of the tag lines due to myocardial contraction. The tag lines, created right after the R-wave, tend to fade during the cardiac cycle due to T_1 relaxation, but for normal resting heart rates (e.g., 60–70 beats/min) the tag lines can persist long enough to allow visualization of cardiac motion over nearly the entire R-to-R interval. Importantly, tag lines in the ventricular blood pool disappear very quickly because of the rapid motion and mixing of blood in the ventricle; this effect is then useful for clearly defining the endocardial borders.

24.3.4 Myocardial Perfusion

Myocardial blood flow is assessed using very rapid MR imaging of the heart during the first passage of an administered contrast agent through the heart. T_1 changes in the myocardium are directly proportional to the contrast agent concentration in the blood or tissue [30, 31], so that through the use of T_1-weighted imaging techniques, myocardial territories affected by a coronary artery lesion can be both qualitatively and quantitatively evaluated. Furthermore, the myocardial territory affected by a coronary artery lesion may or may not show a perfusion deficit under resting conditions; however, during an imposed pharmacological stress, a stenotic vessel cannot respond (dilate) like a healthy vessel resulting in *vascular steal*, a phenomenon in which increased blood flow to the myocardium is supplied by nonstenotic vessels [32]. Consequently, the relative blood flow is reduced through stenotic vessels resulting in a detectable perfusion deficit in the images; as such, both areas of reversible and nonreversible (scar) defects can be represented [33].

First pass perfusion imaging in typically performed using multislice fast gradient-echo imaging with saturation-recovery magnetization preparation obtained during the rapid administration (7 ml/s) of a small contrast agent dose (approximately 0.04 mmol/kg for the extracellular gadolinium agent Gd-DTPA). A saturation-recovery magnetization preparation consists of a nonslice selective 90° radiofrequency pulse, followed by a gradient crusher pulse designed to dephase the transverse component of the magnetization [34]. This preparation drives the magnetization into a well-defined state, permitting the acquisition of a T_1-weighted GRE signal that is independent of the properties of any previous relaxation delay, thus preventing fluctuations in the image signal intensities due to variations in the heart rate or ECG trace. Nevertheless, imaging is typically performed throughout the duration of 40–50 heart beats to adequately capture the first pass of the injected contrast agent through the heart. With currently employed clinical 1.5 Tesla MRI scanners (with state-of-the-art gradient coils and amplifiers producing gradient field amplitudes of 20–40 mT/m with slew rates up to 150 mT/m/s), this imaging can be done in approximately 3–4 slices for every heart beat, with an in-plane image resolution of 2 mm or better.

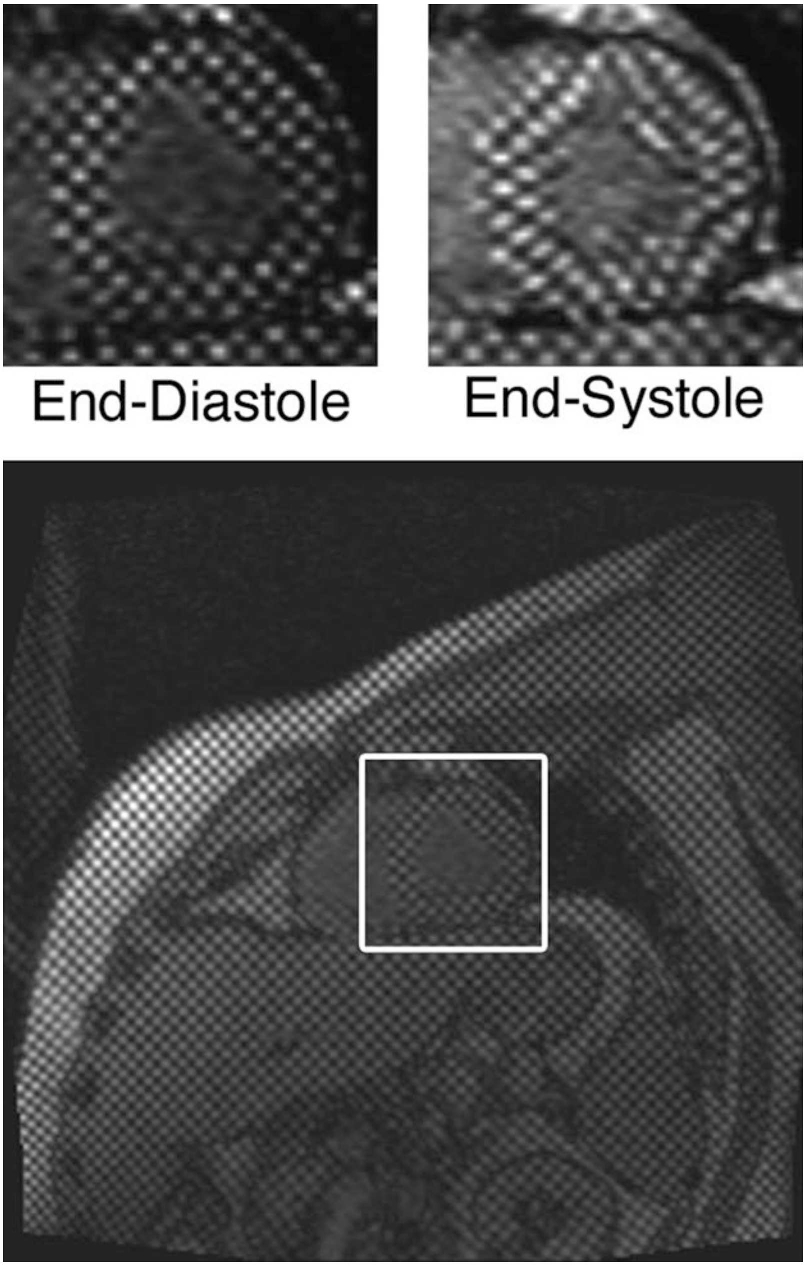

Fig. 24.6 Images with spatial modulation of magnetization in the form of vertical and horizontal stripes in a human volunteer. The grid-tag lines spaced 6 mm apart were created immediately after the R-wave of the ECG. The *upper left panel* shows a magnified view of the heart during this initial phase. A second image is shown on the *upper right* for an end-systolic phase, with the distortion of the tag lines due to cardiac contraction clearly apparent. The tagging technique is equivalent to the implantation of intramyocardial markers. Tracking of the tag lines over the cardiac cycle allows determination of myocardial strains, and has been shown to provide a sensitive method for assessing regional wall motion abnormalities

Qualitative analyses of perfusion studies can be made by viewing the sequence of images as a movie loop, and then visually grading the rate of contrast enhancement in myocardial segments. However, qualitative assessments are highly observer-dependent and thus are also subjective to misinterpretation based on image artifacts or variations in the image brightness due to the inhomogeneous detection of the MR signal by the surface coils. Therefore, in the future, a more quantitative technique based on the time course of signal intensity in the different myocardial segments of interest can provide an objective and robust method of analysis (Fig. 24.7).

24.3.5 Myocardial Viability

The ability to distinguish nonviable myocardium is of critical importance in the management of patients with both acute and chronic coronary artery disease syndromes, yet this is complicated by the presence of reversibly damaged and infarcted myocardium. Until very recently, thalium single proton emission computed tomography (SPECT) and positron emission tomography (PET) were the primary tools for evaluation of myocardial viability. However, with the development of delayed contrast-enhanced MRI (ce-MRI), the cardiac MRI method has quite dramatically and rapidly

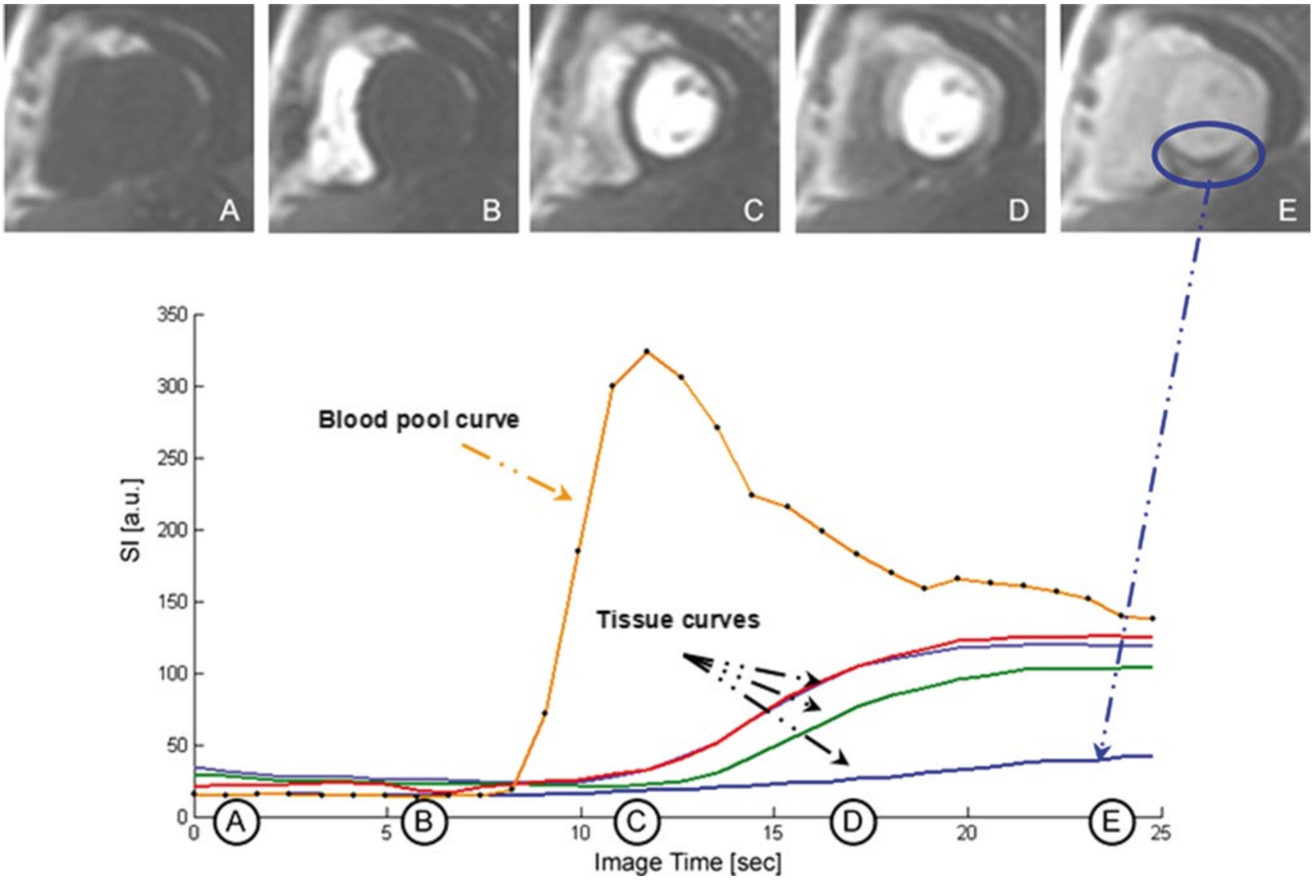

Fig. 24.7 A sample of images acquired using a fast T_1-weighted gradient echo sequence during a bolus injection of 0.04 mmol/kg of the extracellular contrast agent Gd-DTPA is shown, with the resulting signal intensity curves for the left ventricular blood pool and several myocardial segments below. The first image in the series (*A*) shows a short-axis image of the heart prior to injection of the contrast agent. Following injection, the contrast agent quickly enters the right ventricle (*B*) and left ventricle (*C*) and then passes through the coronary and microcirculation (*D*, *E*) causing signal enhancement throughout the myocardium. This example shows a clear perfusion defect in the inferior wall of the left ventricle which can be seen in images *D* and *E* (*circled*) and also the corresponding tissue curve immediately following the first pass of the contrast through the left ventricle

ascended into the forefront of viability imaging [35, 36]. In general, this technique has been shown to identify irreversibly damaged myocardium in both acute and chronic settings following a myocardial infarction and, in tandem with cine imaging, can be used to consistently predict reversibly damaged tissue that may benefit from revascularization and/or other therapies [37, 38]. Furthermore, with the availability of substantially higher spatial resolution than nuclear techniques, ce-MRI can detail the transmural extent of irreversibly damaged tissue and detect both small and large subendocardial defects not identified by either SPECT or PET [39, 40].

So-called *delayed ce-MRI* is performed following the intravenous administration of a gadolinium-chelate contrast agent; typical dosages for imaging viability are on the order of 0.1–0.2 mmol/kg. The contrast agents more readily cross the cell membrane due to the severe myocardial injury and loss of viability [33, 35, 41, 42]. After an appropriate delay (approximately 10–15 min), the contrast agent achieves approximate distribution equilibrium, and loss of functional viability and subsequent leakage of contrast agent result in T_1-weighted signal enhancement because the distribution volume of the contrast agent is larger in the injured tissue compared to normal. Such imaging is typically performed under resting conditions using a breath-hold “inversion recovery” prepared and T_1-weighted segmented GRE sequence. The appropriate inversion delay time following the inversion pulse (approximately 250 ms or less) results in signal nulling of viable myocardium. Note that, for the best results, appropriate inversion delay times are iteratively chosen for each patient. This results in images where the normal viable myocardium is dark, nonviable, fibrotic, or scarred tissue has dramatically increased (hyperenhanced) signal intensity (Fig. 24.8). Typically, one or two signal averages are

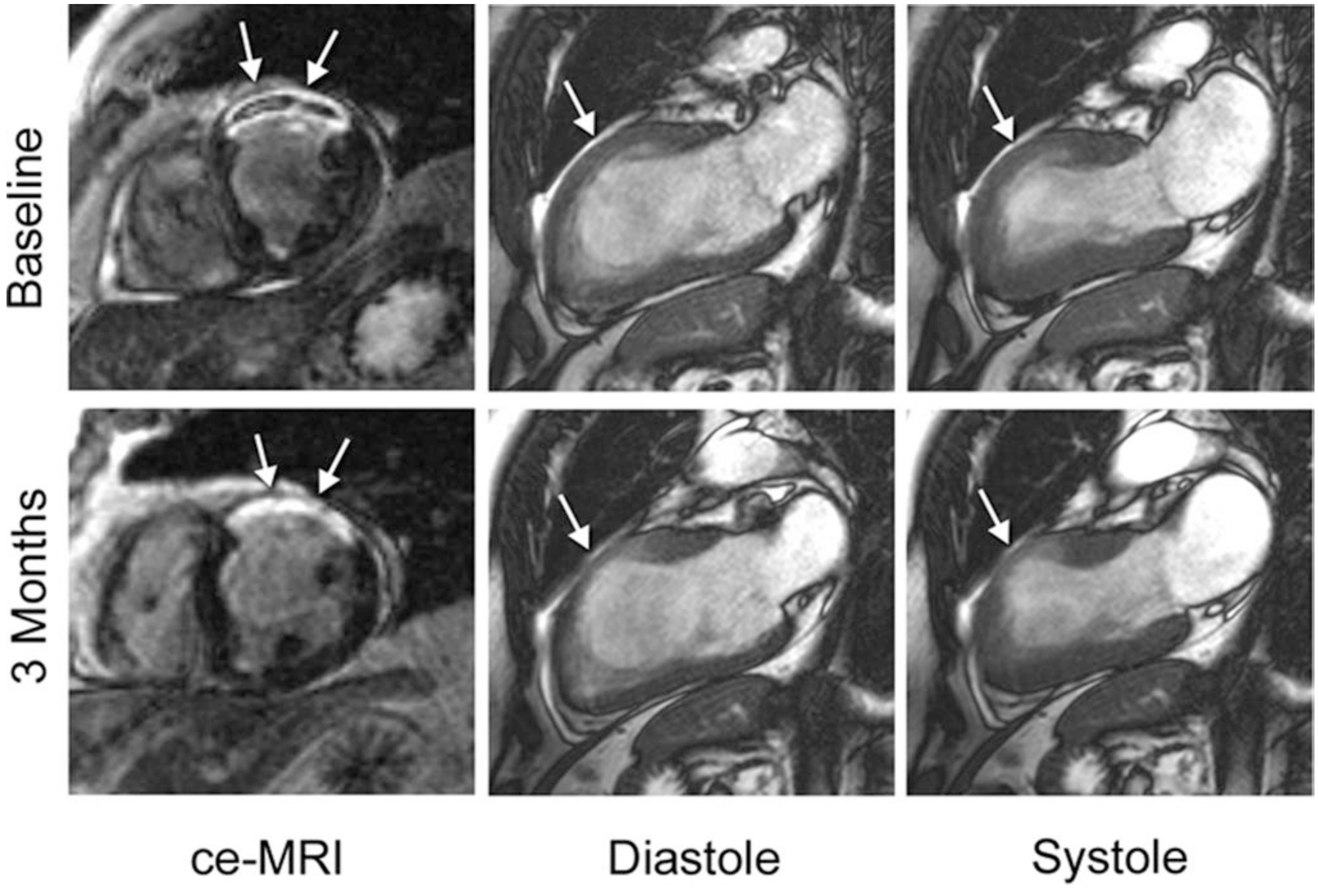

Fig. 24.8 Example of an initial and follow-up MRI exam comparing the region of infarction (*arrows*) with wall thickness and contractility. The acute study at 2 days (*top*) shows evidence of microvascular obstruction within the infarct and reduced wall thickening in the anterior region, shown here by long-axis cine images. During the 3-month study (*bottom*), there is no longer a sign of microvascular obstruction within the infarct territory, diastolic wall thickness has decreased, and contractility has improved in regions adjacent to the infarcted territory

used with an in-plane image resolution of approximately 1.5 mm; this approach as a 2D sequence requires multiple breath-holds to encompass the left ventricle and can be typically accomplished in less than 10 min. In addition, 3D approaches can also be used which cover the entire ventricle in a single, yet longer breath-hold with comparable, but not as good, image quality.

While the delayed ce-MRI sequence is the most widely accepted approach for viability imaging with MRI, there are other less popular techniques that should be mentioned (e.g., imaging with the use of a manganese-based contrast agent). Manganese is a Ca^{++} analog which is actively taken up by viable cells, thus in obtaining T_1-weighted images, viable tissue is enhanced (bright) while nonviable tissue remains dark [43]. Manganese contrast agents are not currently being used in clinical cardiac imaging; however, this may provide an effective alternative method in the near future. MRI of sodium or potassium are also effective methods with potential for imaging viability, but their use remains strictly a research tool due to the very limited availability of multifrequency MRI scanners for clinical use [44].

24.3.6 Blood Flow Velocity

A recorded MR signal can be represented in terms of a magnitude and a phase component. As such, MRI images can be analyzed to elicit the spatial variations of the signal magnitude, but it is also possible to create maps showing the spatial variations of the signal phases. Furthermore, it has been shown that the phase of the signal is sensitive to the velocity of tissue or blood. The so-called phase *contrast MRI technique* uses the phases of the signals to measure relative velocities. For an in-depth discussion of these methodologies, we refer the reader to the literature. Yet, an example of a phase contrast flow velocity measurement in an aorta is shown in Fig. 24.9, which has been used to calculate pulse wave velocities for measuring vessel stiffness [45].

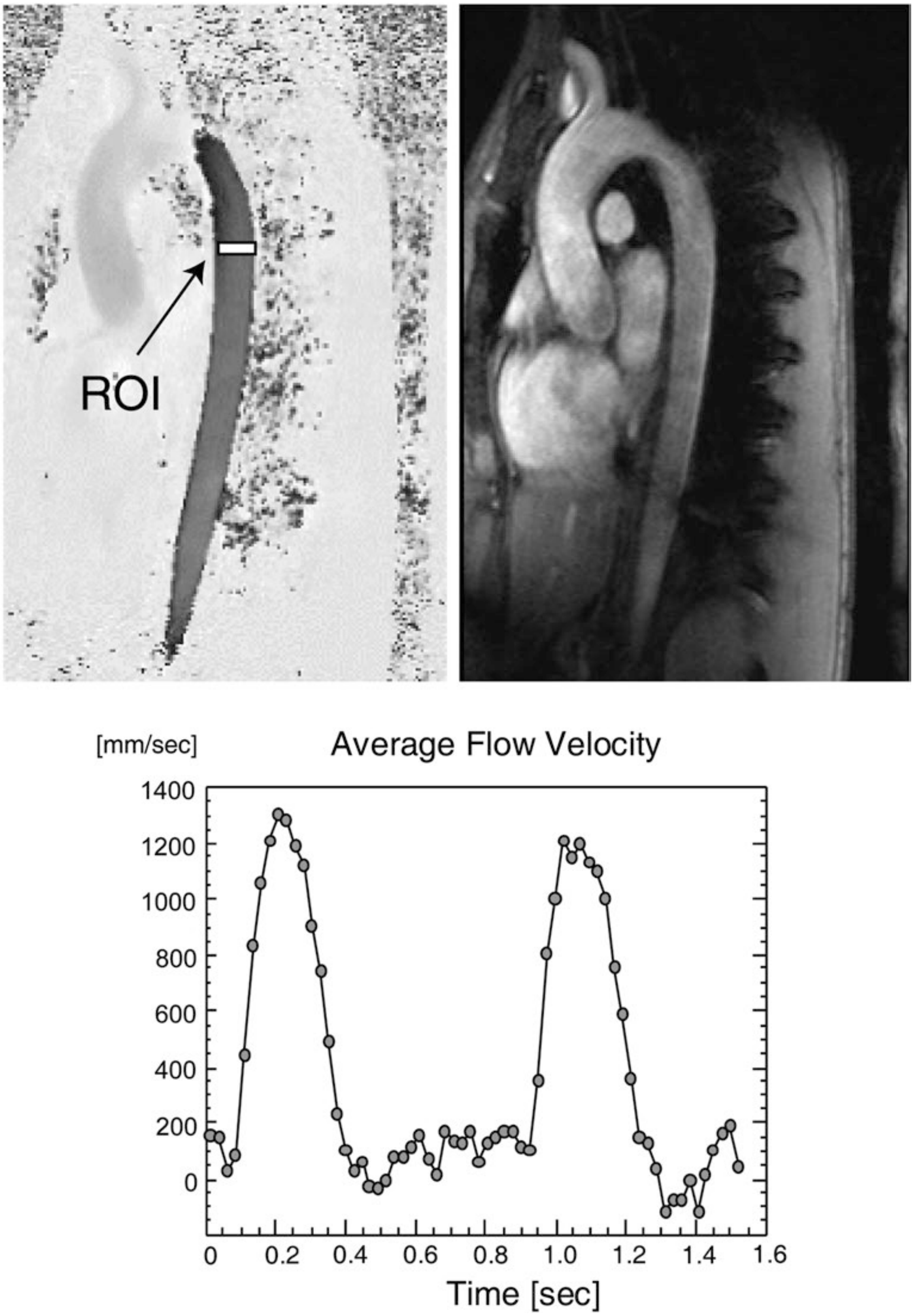

Fig. 24.9 Phase contrast imaging of the aorta in a human volunteer. Both the magnitude and phase images are shown. Images were acquired for X cardiac phases, covering approximately 2.5 heart beats. A region of interest (*white box*) was placed on the phase images in the thoracic aorta to determine the variation of flow velocity in the vertical direction of the image plane. The variation of the velocity is shown in the graph. *ROI* region of interest

24.3.7 Fiber Structure

24.3.7.1 Importance of Myofiber Orientation

The analysis of myocardial microstructure continues to be considered an important factor in better understanding underlying pathologies and/or associated arrhythmias. This is due to the fact that structural fiber arrangement is modified over the time course of various cardiomyopathies. In the healthy heart, it is generally accepted that cardiac muscle fibers or myofibers are arranged as counter-wound helices encircling the ventricular cavities and where fiber orientation is a function of their transmural location [46–48]. Further, myofibers are predominantly organized in the base–apex direction at the epicardial and endocardial surfaces, and rotate to a circumferential direction in the mid-wall. This counter-wound helical structure is considered to be responsible for the torsional or wringing motion of the left ventricle which serves three main mechanical functions: (1) equalizing myofiber strain and workload; (2) optimizing the volume of blood ejected during systole (stroke volume); and (3) storing torsional energy in the intracellular and extracellular matrix, and when released, increasing ventricular filling during diastole [49–56]. Therefore, cardiac fiber orientation can also be considered as one of the primary determinants of ventricular pump function.

24.3.7.2 Quantifying Fiber Structure with Diffusion Tensor MRI

More recently, *diffusion tensor MRI* (DTMRI) has been developed and employed as a nondestructive means to quantify 3D ventricular fiber orientation [46, 57–60]. The underlying principle in determining cardiac fiber orientation by DTMRI is that the fastest direction of water diffusion corresponds to the local myofiber orientation. Therefore, by obtaining a series of diffusion-weighted images, the effective diffusion tensor of water in the myocardium can be estimated using a relationship between the measured echo attenuation in each imaging voxel and the applied diffusion sensitizing gradient [61]. As such, diffusion-weighted pulse sequences are designed such that molecular displacements in the direction of the applied diffusion sensitizing gradients will attenuate the echo signal, thus enabling the estimation of water diffusivity in a given direction. The strength of the diffusion weighting or *b*-value usually ranges from 500 to 1500 s/mm^2 in cardiac DTMRI. The diffusion tensor, which is a symmetric 3×3 second rank tensor, is determined for each imaging voxel and represents the net 3D diffusion in the tissue. In order to determine the required six independent parameters of the diffusion tensor, at least seven images must be obtained for a given slice—six diffusion-weighted images applied in six noncolinear directions and one diffusion-independent image. However, it is also common to estimate the diffusion tensor by obtaining many diffusion-weighted images varying in direction (12–16 directions) and *b*-value, where the best fit for the diffusion tensor can be determined using multilinear regression. Nevertheless, ventricular fiber orientation can be obtained with DTMRI due to the anisotropic nature of water diffusion in the myocardium [62]. The fastest direction of diffusion or primary eigenvector of diffusion has been validated to coincide with the local longitudinal myofiber orientation, as water diffusion in the cross fiber directions is restricted by the cellular borders and laminar sheets in the myocardium [63, 64]. Note that the secondary and tertiary eigenvectors of diffusion correlate with the laminar sheet direction and sheet normal, respectively [58, 65, 66].

From a research perspective, it is also interesting to note that DTMRI can be used to obtain fiber orientation both in vivo or ex vivo [67, 68]. In addition, it has been shown that DTMRI can successfully be performed on isolated human hearts if collected within 3 days postmortem from the donor [69]. Currently, cardiac DTMRI is primarily used as a research tool, and is not a routinely employed cardiac MR protocol in a clinical setting. Today, this imaging technique does not contribute to the diagnosis of cardiomyopathies, or provide information that can be used to determine patient treatment options. However, in concert with myocardial tagging, in vivo DTMRI does provide valuable insights into the myofiber structure–function relationship in the ventricles in both normal and diseased states as discussed in Sect. 24.3.7.3. In general, the spatial resolution of diffusion imaging is dependent on the diffusion sensitizing pulse sequence and magnetic strength of the scanner. For example, for in vivo diffusion imaging of large mammalian hearts in a 1.5 Tesla magnetic field, a spatial resolution of approximately 3×3×3 mm can be expected [70]. For ex vivo diffusion imaging with high field MRI scanners (3–9.4 Tesla), a spatial resolution less than 1×1×1 mm can easily be obtained. An example of ex vivo DTMRI of a freshly cardiopleged and isolated human heart is shown in Fig. 24.10. The raw diffusion images are shown along with the fiber orientation projected into the imaging plane as determined by the primary eigenvector of diffusion for a mid-ventricular slice. Furthermore, Fig. 24.11 shows a 2D contour plot of the fiber inclination angle α of a healthy human heart fixed directly postmortem using the methodologies described in Eggen et al. [69].

24.3.7.3 Pathological Changes in Fiber Structure

It was reported that by using cardiac DTMRI in conjunction with phase contrast strain-rate imaging, Tseng et al. were able to determine that a state of fiber disarray exists in hypertrophic cardiomyopathy which results in a disordered pattern of principle myocardial shortening. In the same study, these investigators observed that a positive correlation exists between fiber disarray and myocardial hypokinesis [70]. Additionally, several studies have attempted to quantify cardiac fiber architectural remodeling after the occurrence of myocardial infarction [71, 72]. In these reports, fiber disarrays and increases in diffusivity were evident in the infarcted regions; this was considered to be consistent with abnormal wall motion and/or cell death. More recently cardiac DTMRI has played a key role in developing computational approaches to investigating the electromechanics of healthy and diseased hearts, which are becoming necessary for the comprehensive understanding of cardiac function [73]. Such sophisticated models have provided important insights into arrhythmia induction in peri-infarct zones surrounding necrotic scar in chronically infarcted canine hearts [74].

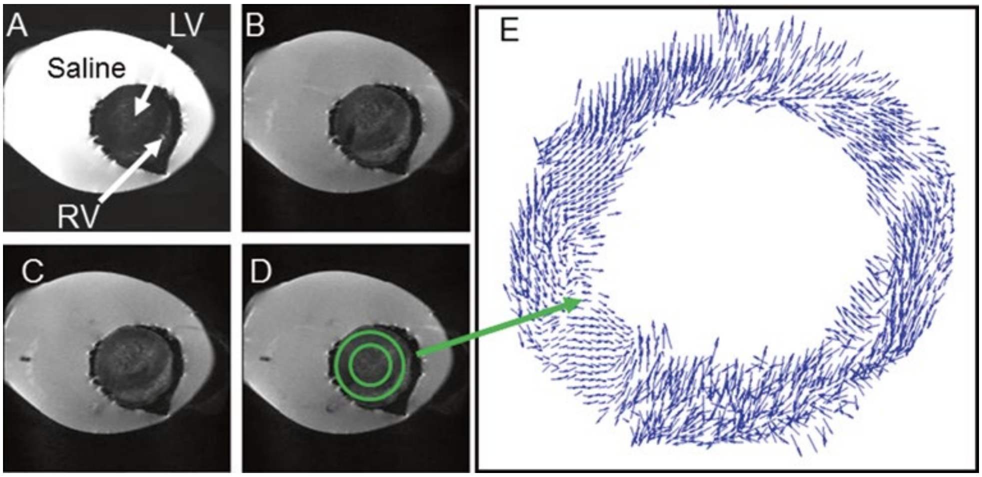

Fig. 24.10 Diffusion tensor MRI imaging of a freshly excised normal human heart. The unfixed heart was submerged in saline and all air was removed prior to imaging. For the determination of cardiac fiber orientation, six diffusion-weighted images were acquired with one nondiffusion-weighted image (**A**) at the mid-ventricular level. Three diffusion-weighted images are shown (**B**–**D**) acquired with diffusion gradients applied in three orthogonal directions. The left ventricular fiber orientation is projected onto the imaging plane (**E**) as determined by the primary eigenvector of diffusion or direction of fastest diffusion. Imaging parameters were as follows: field of view = 180 × 180 mm, matrix = 196 × 196, and in-plane spatial resolution = 0.9 × 0.9 mm, *b*-value = 1000 s/mm^2; the slice thickness was 3 mm. *LV* left ventricle, *RV* right ventricle

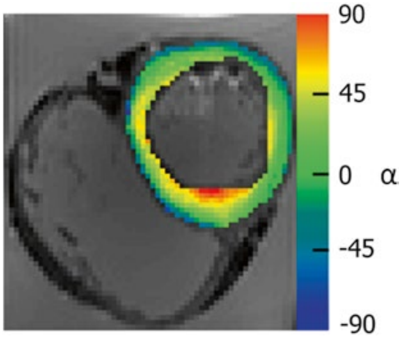

Fig. 24.11 2D contour plot of the fiber inclination angle α in a healthy human heart fixed directly postmortem. The short-axis image was obtained from the mid-level of the left ventricle

24.4 MRI and Biomedical Devices

24.4.1 Real-Time Imaging and Cardiovascular Interventions

To date, X-ray-based fluoroscopic techniques have been the gold standard for most invasive diagnostic and/or therapeutic applications relative to the heart. However, with the advent of ultrafast MRI and the development of MRI-compatible catheters and guide wires, the goal of achieving real-time guidance by MRI for cardiovascular interventions is emerging as a new alternative [75]. More specifically, the use of MRI for guided interventions would minimize or even eliminate reliance on ionizing radiation and iodinated contrast agents, an advantage particularly for pediatric patients. To date, continuous improvements of MRI techniques and MRI scanner hardware have rendered it feasible to achieve the relative clinical fluoroscopic image rates of 5–15 images/s [76]. Thus, it is considered highly probable to use MRI for guiding interventional cardiovascular procedures, such as coronary catheterization [77] and cell or gene therapy delivery [15], with close to real-time image refresh rates. Initial interventional studies with MRI guidance have demonstrated the advantages of MRI, including: (1) the ability to image arbitrarily oriented cross-sections; (2) interactive steering of the image plane; and (3) excellent soft tissue contrast for the detection and visualization of lesions [78].

Several other technical advances have also been considered as crucial for advancing the possibility of performing interventional procedures under MRI guidance, including: (1) development of 1.5 Tesla magnets with short bores that allow access to the groin area for catheter-based procedures; (2) LCD monitors that can be exposed to high magnetic fields to allow the operator to perform an intervention and control MRI scan parameters from a position right next to the magnet; and (3) development of catheter-based MRI antennae for localized intravascular signal reception and high-resolution imaging [79].

For MRI-guided cardiac interventions, one of the basic requirements is to visualize and track the catheters and devices used in the therapies while they are manipulated through the heart and vascular spaces [80]. In general, catheter tracking techniques can be divided into two categories—active and passive. Active tracking of catheters and devices requires the instrument to receive or send a signal in order to identify its relative location. For example, a receiving coil can be incorporated into the device and thus connected to the scanner such that the position can be located based on the frequency of the received signal from the body coil. MRI-guided active catheter tracking used for real-time 3D intracardiac navigation, mapping, and ablation has been successfully demonstrated in work by Gaspar et al. [81]. Passive tracking of catheters involves creating a signal void without interfering with the image quality of the tissue being imaged. This latter method can be achieved through the choice of materials incorporated into the catheter or device. For example, small amounts of titanium, gold, or copper can be deposited into the catheter tip in order to introduce a susceptibility artifact such that the tip of the catheter can be continuously tracked. The details of one passive design of a deflectable guiding catheter constructed from nitinol and Kevlar is further described in Bell et al. [82].

A recent development in the emerging field of MRI-guided cardiac interventions is the real-time delivery of transcatheter valves. Recently, McVeigh et al. demonstrated that a transcatheter bioprosthetic aortic valve could be delivered via a direct approach through the left ventricular apex in approximately 90 s with real-time interactive MRI guidance [83]. Importantly, immediately after the procedure, myocardial perfusion, blood flow through the valve, and ventricular function were assessed with MRI in order to verify proper placement of the valve. It is considered that this minimally invasive MRI-guided aortic valve replacement technique may prove to be a less morbid approach than conventional valve replacement surgeries, and thus may have added benefits for the very ill and/or elderly patient population. Research in swine has also proven the feasibility of a trans-arterial aortic valve implantation using a commercially released valve (CoreValve®, Medtronic, Minneapolis, MN, USA) and a modified delivery system [84].

To date, other reported MRI-guided cardiac interventions and applications include, but are not limited to [80, 85]: (1) diagnostic cardiac catheterization; (2) electrophysiological recording/radiofrequency ablation [81, 86]; (3) balloon dilation and stent placement [87]; and (4) atrial septal defect closure. For an in-depth discussion of the advantages and difficulties associated with these MRI-guided cardiac interventions, we refer the reader to the growing body of related literature (see also Chaps. 32 and 36).

24.4.2 MR-Conditional Implantable Devices and Nomenclature

Today, most implantable cardiac devices contain metallic parts that can interfere with MR cardiac imaging and/or pose potential safety risks for the patient. Such potential interactions can include mechanical effects from the static magnetic field that could cause movement or dislodgement of an implanted device, or device heating due to the RF field and gradient magnetic field. For example, when scanning patients with cardiovascular implantable electronic devices (CIEDs) such as pacemakers or implantable cardioverter-defibrillators (ICDs), there is a potential risk of increasing the pacing threshold because of lead tip heating, due to the RF and gradient magnetic field. Even though there are potential risks of scanning patients with such devices, it can still be permissible to conduct an MRI scan under certain conditions. Importantly, implantable devices with demonstrated safety in the MR environment within defined conditions are referred to as *MR-conditional*, whereas devices that pose no known hazards resulting from exposure to any MR environment are termed *MR-safe* [88]. An MR-safe item is typically composed entirely of electrically nonconductive, nonmetallic, and nonmagnetic materials; most cardiac implantable devices do not fall into this category. Lastly, devices which pose unacceptable risks to the patient, medical staff, or other persons within the MR environment are termed *MR-unsafe*.

Until recently, CIEDs such as pacemakers or ICDs were a strict contraindication to MRI. The potential interactions of a CIED with the MR environment include, but are not limited to [89]

- Mechanical movement of the device or lead dislodgment (static magnetic field interaction)
- Lead tip heating (RF and gradient magnetic field interaction)
- Current induction leading to rapid pacing (RF and gradient magnetic field interaction)
- Over-sensing and under-sensing the cardiac EGM (RF and gradient magnetic field interaction)
- Reed switch interference (static magnetic field interaction)
- Electrical reset or permanent device damage (static, RF, and gradient magnetic field interaction).

Recently, the risks of these potential hazards have been minimized by specially engineering CEIDs to be MR-conditional. In a randomized, prospective, controlled worldwide clinical trial, patients ($n = 464$) were randomized to undergo an MRI scan between 9 and 12 weeks postimplant (MRI group, $n = 258$) or not to undergo MRI (control group, $n = 206$) after successful implantation of a specially engineered dual-chamber pacemaker and leads. MR imaging was performed under the following conditions: static magnetic field strength of 1.5 T, maximum SAR value of 2 W/kg for each sequence, and a maximum gradient slew rate of 200 T/m/s. In addition, only head and lumbar sequences were performed such that the isocenter of the RF transmitter coil was above the C1 vertebra and below T_{12}. The results of the study demonstrated that no MRI-related complications occurred during or after MRI, including sustained ventricular arrhythmias, changes in pacing thresholds or sensed EGMs, pacemaker inhibition or output failures, electrical resets, or other pacemaker malfunctions [90]. This pacemaker (EnRhythm MRI system, renamed RevoMRI™ SureScan® system, Medtronic) received Conformité Européenne (CE) mark in 2008, and was approved for use in the USA in 2011. Although CIEDs have been specially engineered to be MR-conditional, the problem remains to be very complex. For example, the potential hazard of lead tip heating, which can lead to an increase in pacing threshold, is dependent on many parameters including [91]:

- Patient size
- Anatomy
- Body composition
- Position in the bore
- Scan sequence
- Lead routing
- Lead design.

Because of these complexities, computer-aided modeling has been used as a practical and efficient method for exploring millions of variable combinations in a holistic manner [91].

It should be noted that a device may be MR-conditional, but that does not necessarily mean it is "MR-compatible." MR-compatibility is used to describe the interaction of the device with the diagnostic quality of the MR image. In the example of the MR-conditional pacemaker, researchers have found that high-quality CMR images for the assessment of cardiac anatomy and function can be obtained in most patients with an implantable pacing system [92]. Furthermore, new scan sequences have been proven effective at reducing artifacts in patients scanned with ICDs [93].

It is foreseen that a new set of MRI safety concerns may arise when such imaging is performed using intravascular coils [94, 95]. Such intravascular coils may, for example, be used to examine vulnerable plaque on vessel walls; localized heating in the vicinity of the coil could disrupt the plaque, thus causing catastrophic consequences. Note that heating strongly depends on the wavelength (MRI frequency), geometry of the body and the device, and placement of the body and device with respect to each other and within the MR system. On the other hand, one could also foresee potentially using this heating phenomenon to induce therapy itself (e.g., tumor ablation to lesion formation). For further information on MR-conditional and/or MR-compatible biomedical devices and additional contraindications for cardiac MRI exams, we refer the reader to the growing body of literature on this topic.

24.4.3 Assessment of Biomedical Device Performance

Cardiac MRI also provides a unique opportunity to test, in vivo, the performance of implanted devices such as prosthetic heart valves and heart pacing devices (those that would be considered both MRI-compatible and safe). For example, in patients with artificial aortic valves, the flow downstream from the implanted valve may be severely altered. These changes have been associated with an increased risk of thrombus formation and mechanical hemolysis. Therefore the capabilities of MRI velocity mapping would be considered very useful for the noninvasive evaluation of the flow profiles in patients with a mechanical valve prosthesis [96, 97]. For example, in one report, Botnar et al. found that peak flow velocity in the aorta was significantly higher in patients with valvular prosthesis than in normal patients [98]. In that same study, the investigators also reported that diastolic mean flow was negative in patients after valve replacement, but not in controls. Furthermore, in instances where real-time MRI is used to guide the placement of a stented artificial valve, an assessment of the flow profile can be obtained immediately to determine the relative success of the implant procedure.

The usefulness of MRI for assessing the function of cardiac pacing devices has already been proven in experimental animal studies [99], with early feasibility data obtained in humans using MR-conditional pacemakers [92]. For example, in our laboratory, we have quantified pacing-induced left ventricular dyssynchrony in swine paced from the right ventricular apex, a standard pacing lead implant site, using MR tissue tagging. Figure 24.12 demonstrates that right ventricular apex pacing alters the mechanical activation pattern of the left ventricle, resulting in circumferential stretch in the lateral and posterior walls and regional variations in circumferential shortening in end-systole (see also online Video 24.1). Our lab has also demonstrated intraventricular dyssynchrony during right ventricular apical pacing in an isolated human heart [100]. Furthermore, the myocardial strain in a normal swine heart and healthy human volunteer can be viewed in real time in online Videos 24.2 and 24.3.

24.5 Quantitative Analyses of Cardiac MR

It is important to note that post-processing of cardiac MRI studies represents the stage at which the full potential of the cardiac MRI examination may be best realized. Post-processing is comprised of two major steps, namely image post-processing and data post-processing. The first step largely involves segmentation algorithms to delineate and extract features and structures of interest from the collected images. The second step consists mainly of applying mathematical and statistical methods to aid in diagnosis.

For many cardiac investigative protocols, the myocardium is the area of interest for analysis, so one needs to segment the myocardium from the rest of the image to extract further information, e.g., utilize contrast enhancement in a perfusion study or monitor systolic thickening of the wall for a MR cine study.

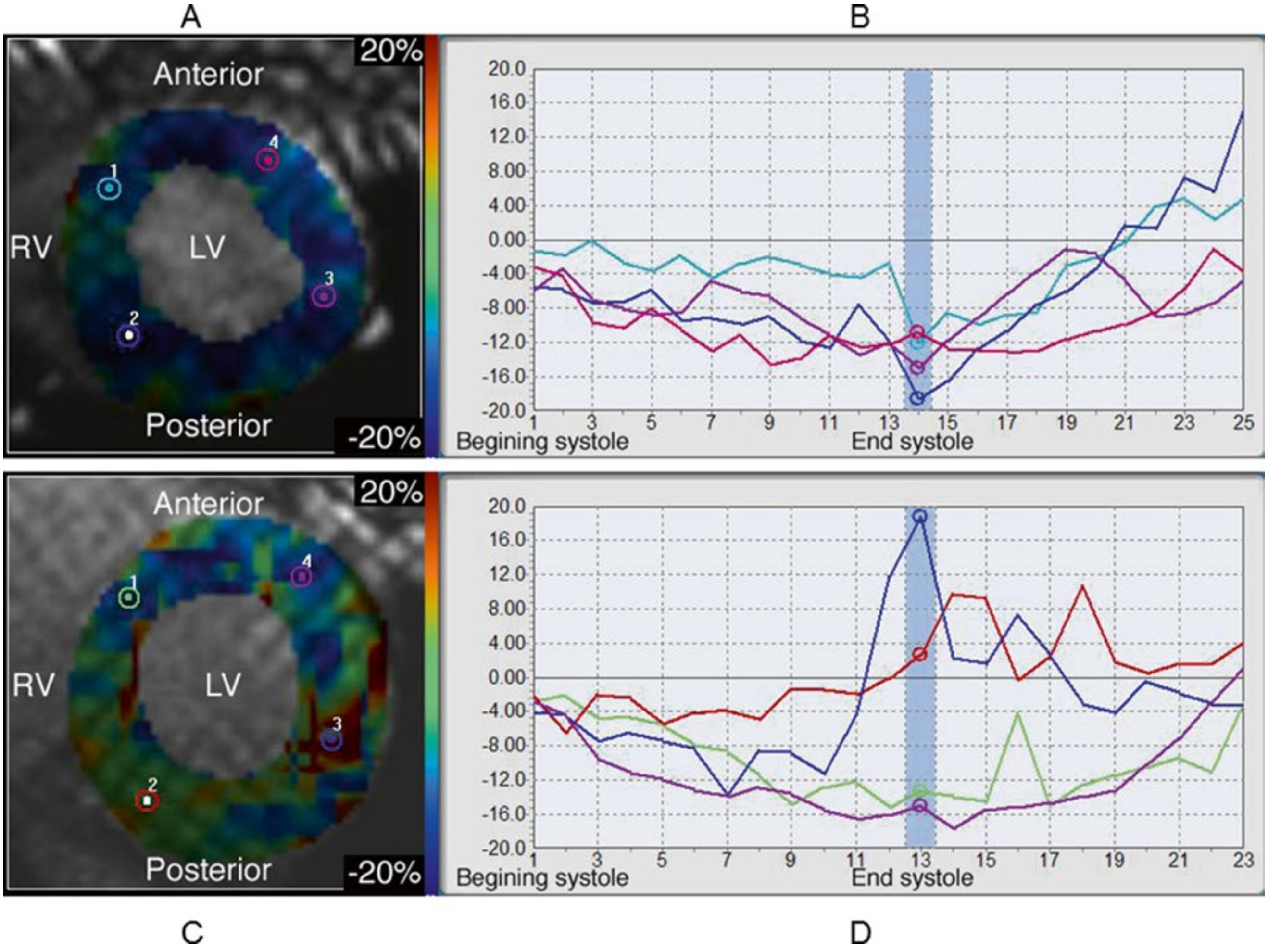

Fig. 24.12 Circumferential strain quantified by MR tissue tagging in a normal porcine heart (**A**–**B**) and after 6 weeks of cardiac pacing from the right ventricular apex in the same heart (**C**–**D**). Graphs (**B**) and (**D**) plot the circumferential strain values throughout the cardiac cycle prior to pacing and after 6 weeks of pacing at the specified probe locations in (**A**) and (**C**) respectively. Pacing from the right ventricular apex caused regional disarray in cardiac strain in the left ventricle at end-systole (**C**) and throughout the cardiac cycle (**D**), in comparison to the same heart 6 weeks prior to the onset of pacing (**A**–**B**). Right ventricular apex pacing induces left ventricular dyssynchrony and results in poor left ventricular pump function. *LV* left ventricle, *RV* right ventricle

24.5.1 Ventricular Function

Quantitative analyses of relative ventricular function are also based on the segmentation of the myocardium. In general, this is achieved by drawing contours on the endocardial and epicardial borders of the myocardium (Fig. 24.13). In general, the ventricular volumes of interest are the end-diastolic and end-systolic volumes, as well as derived parameters such as the stroke volume and ejection fraction. Although ventricular volumes have been computed from differently orientated views of the heart, analyses of the short-axis views are most widely used in cardiac MRI due to their proven accuracy [101–104]. In the simplest case, myocardial segmentation is performed only for the images corresponding to the end-diastolic and end-systolic phases. The end-diastolic phase is defined as the phase containing the largest blood pool area in the left ventricle, whereas the end-systolic phase is identified as the image containing the smallest blood pool area (Fig. 24.14).

Once the end-diastolic and end-systolic phases are fixed, the contours are drawn in the images for the end-diastolic and end-systolic phases for all slices containing left ventricle. In images for a basal slice of the left ventricle, parts of the aorta and aortic valve may be visible. It should be noted that inclusion of contours above the mitral valve plane will significantly overestimate the values for myocardial mass and ventricular volume. Thus, the careful inclusion or exclusion of slices near the base of the heart for determination of the volumes at end-diastole and end-systole is of considerable importance for an accurate determination of the relative ventricular volumes. Once all contours are drawn and verified, the ventricular volume can be computed by simple slice

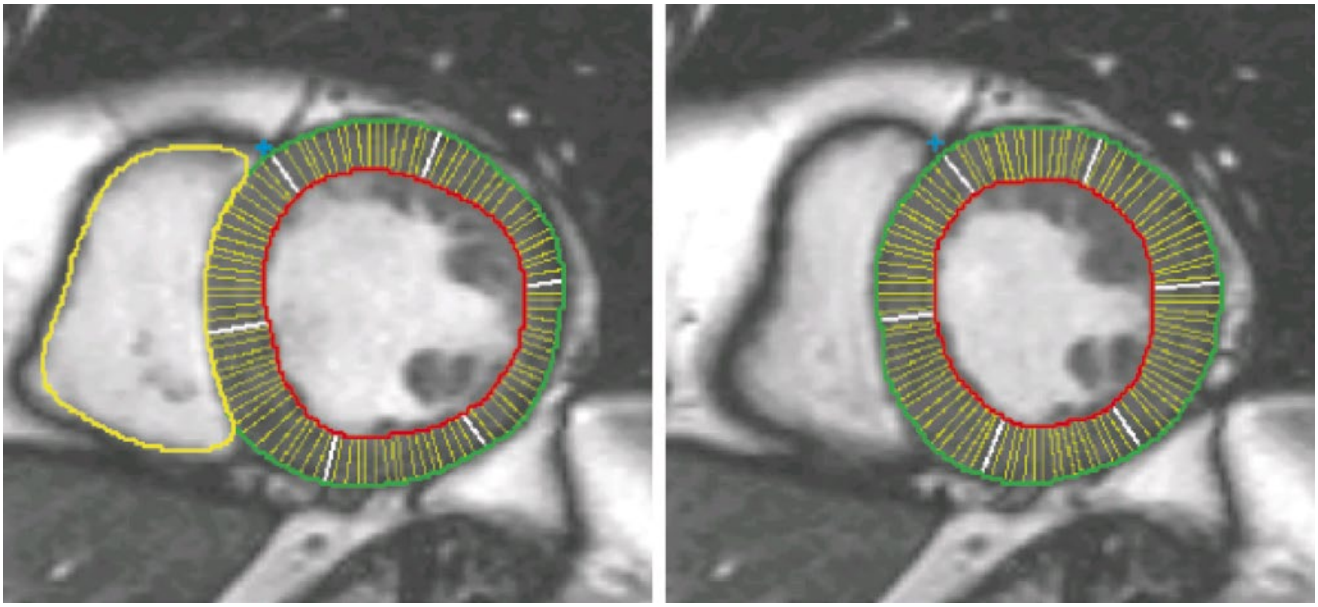

Fig. 24.13 Example of myocardial segmentation for two images corresponding to the end-diastolic (*left*) and end-systolic (*right*) phases in a patient with poor cardiac function. Contours are drawn around the blood pool demarking the endocardium and the epicardium. A contour is also drawn around the right ventricular blood pool. For this particular patient, the cross-section of ventricular cavity with the short-axis view changed significantly less than in a healthy normal. Also shown are chords connecting the endocardial and epicardial borders. The chords are orthogonal to a center line between the two contours. The chords measure the true thickness of the myocardium as opposed to radial chords that emanate from the center of the left ventricle

summation using Simpson's rule with the slice thickness as the increment.

Recently, Young et al. [104] proposed an optimization method for speeding up the process of contour drawing by placing guide points on the endocardial and epicardial borders, instead of drawing continuous contours for both borders. The algorithm then automatically detects the myocardial borders by interpolation between the guide points. This user-friendly method reduces the burden of generating contours compared to the conventional tracing of the contours. Subsequently, Swingen et al. [105] modified the guide point technique by including feedback from continuously updated 3D models of the heart, to evaluate both the placement of guide points and the accuracy of the computed volumes. They showed that the combined use of short- and long-axis views results in more accurate estimates of the ventricular volume and myocardial mass, compared to exclusive reliance on short-axis views [106] (Fig. 24.15).

Common parameters of interest for volumetric analyses are:

- *Left ventricular mass*: The myocardial mass is obtained by multiplying the myocardial volume by the myocardial specific gravity (1.05). Myocardial volume is calculated as the difference between the epicardial and endocardial volumes. The normal mean for left ventricular mass is 92 ± 16 g/m^2 of body surface area.
- *Stroke volume*: The stroke volume is calculated as the difference between end-diastolic and end-systolic blood or chamber volumes, and it represents the volume of blood ejected by a ventricle per heart beat (in the absence of aortic regurgitation). Unless shunts and valvular regurgitation are present, the calculated stroke volumes of the two ventricles should be nearly equal. This is a rule of thumb for verification of the volume computation.
- *Ejection fraction*: This is the ratio of the ventricular stroke volume to the end-diastolic volume. The normal range is between 55 and 65 %. An ejection fraction of less than 40 % is considered to indicate impaired ventricular function.
- *Cardiac output*: This is the product of stroke volume and heart rate. It is a measure of the volume of blood ejected by the heart per beat. For an average adult, cardiac output is 4–8 l/min. Cardiac output is often corrected by normalization with respect to the body surface area.

24.5.2 Analyses of Wall Motions and Regional Myocardial Strains

24.5.2.1 Analyses of Relative Wall Motions

MRI wall motion analyses are typically performed to measure the changes in thickness of the left ventricular wall, from diastole to systole [107–112]. Wall motion abnormali-

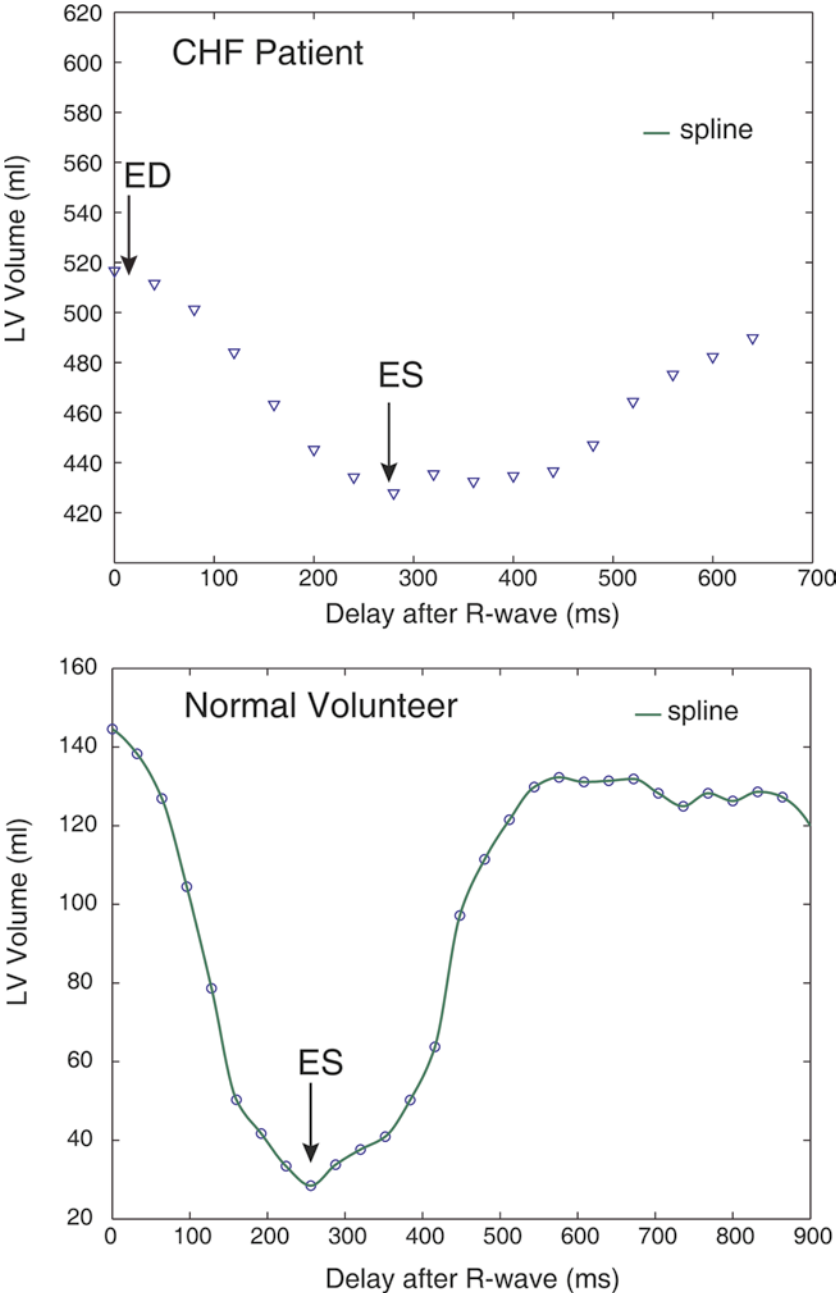

Fig. 24.14 Volume-time graph with the end-diastolic (*ED*) and end-systolic (*ES*) phases. The *upper graph* shows the variation of left ventricular (*LV*) volume over the cardiac cycle for a patient with congestive heart failure (*CHF*), and the *lower graph* is the same type of graph for a healthy volunteer. The CHF patient had an enlarged ventricle (i.e., large volume) and a very low ejection fraction. Because of the low ejection fraction, the curve in the CHF patient is relatively flat. Ventricular volumes were calculated by Simpson's rule from a set of short-axis images. The endocardial border had been traced on each cine frame to obtain a complete left ventricular volume versus time curve

ties are commonly associated with many cardiac diseases, including dilated cardiomyopathy, end-stage valvular disease, and ischemic heart disease.

The assessment of relative myocardial wall thickness, thickening, and wall motion abnormalities proceeds from the MRI segmentation along the endocardial and epicardial borders. For example, a center line can be drawn between the myocardial contours [113]; approximately 100 chords are then drawn orthogonal to the center line at equal intervals to intersect the two myocardial contours (Fig. 24.13). With the center line technique, the chords are optimally placed to measure the exact thickness of the transmural myocardium [113].

Parameters of interest for wall motion analyses include:

- *Myocardial thickness*: The length of the orthogonal chords, from the endocardial to the epicardial borders, measuring myocardial thicknesses.
- *Myocardial thickening*: Differences in end-diastolic and end-systolic thickness, as a percentage of end-diastolic thickness; these are measures of relative wall thickening and can be considered as the radial component of myocardial strain.

24.5.2.2 Analyses of Regional Myocardial Strains with Tagged MR Images

Although the time-consuming analysis of tagged MR images has been a limiting factor for the widespread quantitative analyses of myocardial strains, a recently developed *harmonic phase* (HARP) MR technique permits fast and accurate analyses of strains from MRI-tagging protocols [114–116]. The resultant analyses based on this technique are very fast, accurate, and observer-independent since the myocardial strains are computed from information contained in the images, not the manual operator task of tracking the tag line intersections [117]. Figure 24.16 demonstrates a typical analysis of cardiac circumferential strain in three phases of the cardiac cycle using the HARP technique from data obtained from a human volunteer (HARP, Diagnosoft, Inc., Palo Alto, CA, USA). The circumferential strain values peak at ~20 % in the mid-wall where myofibers are predominately oriented in the plane of the cardiac short axis, consistent with the maximal amount of shortening permissible in a cardiac myocyte.

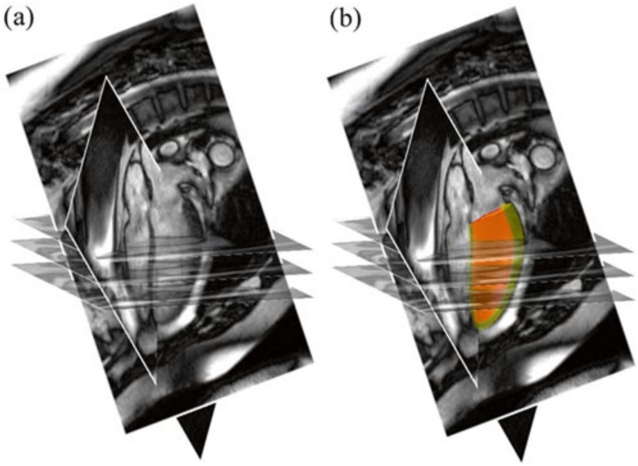

Fig. 24.15 A typical set of TrueFISP slices using a 3D analysis protocol (**a**) with co-registered long- and short-axis images (three of six short-axis images shown for clarity). Image set with 3D model of the left ventricle (**b**)

24.5.3 Perfusion Analyses

Myocardial perfusion is a measure of blood flow (e.g., ml/min) per unit mass of myocardial tissue. Myocardial perfusion should ideally match the demand for oxygen in the myocardium. Commonly, perfusion is assessed at both rest and during stress to evaluate the capacity of the coronary circulation to increase blood flow above its baseline level, and thus match increases in oxygen demand. A ratio of the perfusion parameters, measured at stress and divided by the value for rest, will give a so-called *perfusion reserve*. In healthy individuals, myocardial blood flow increases approximately three to fourfold above its baseline level with maximal vasodilation; with disease, the perfusion reserve decreases, and a flow reserve on the order of 2.5:1 is often used as the cutoff for deciding whether or not cardiovascular disease is present.

Analyses of myocardial perfusion can be carried to different levels of study, depending on the diagnostic needs and clinical resources available. One type of qualitative analysis associated with nuclear imaging is performed by visual comparison of the peak contrast enhancement in different myocardial segments during the first pass of the contrast medium through the left ventricle. The images are often viewed for this purpose in cine mode; delays in contrast enhancement and/or a reduced peak contrast enhancement relative to other myocardial sectors are then interpreted as signatures of locally reduced myocardial blood flow. However, to do this accurately, the absence of image artifacts is important if the analysis is purely qualitative and visual; if this is the case, then no image post-processing is necessary. Nevertheless, a qualitative analysis does have limited capabilities to detect global reductions of myocardial perfusion, especially in patients with multiple vessel coronary artery disease.

Quantitative analyses of MRI perfusion studies commonly start with image segmentation, similar to the procedure used for the analysis of cine studies. First, a technician typically segments one image with good contrast enhancement along the endocardial and epicardial borders of the left ventricle. These contours are then either copied to the remaining images

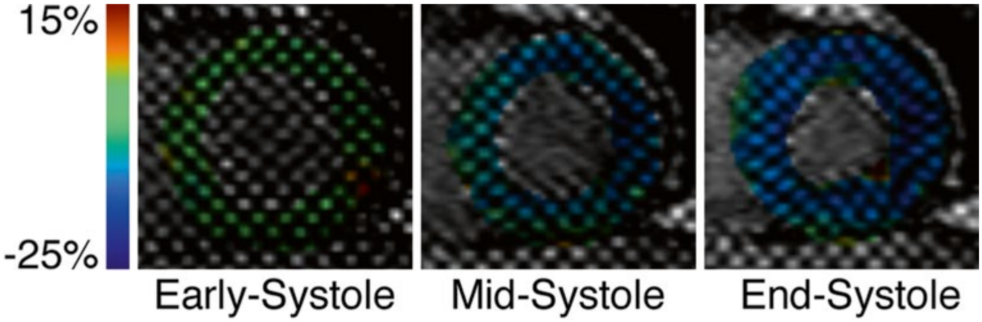

Fig. 24.16 Analysis of cardiac circumferential strain in a human volunteer for three phases of the cardiac cycle using the HARP technique for MR tissue tagging analysis (HARP, Diagnosoft, Inc., Palo Alto, CA, USA). Circumferential strain in the images is indicated by the *color palette*. The grid-tag spacing used in this analysis was 6 mm

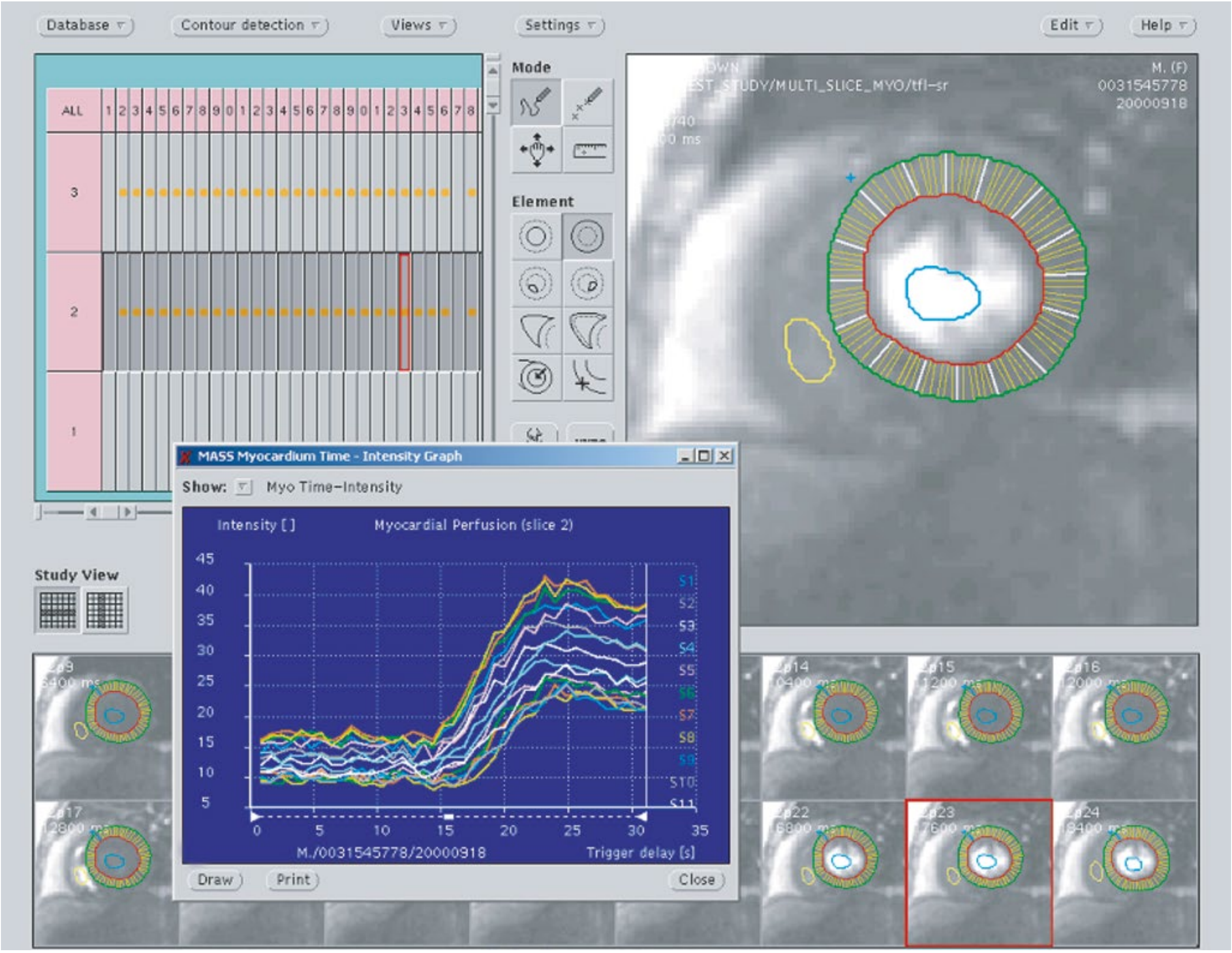

Fig. 24.17 Example of a typical graphical user interface software for analysis of perfusion studies. Segmentation contours are drawn by the user to define the endocardial and epicardial borders. Similar to the approach used for cine analysis, the analysis is carried out on a sector basis; in this case, 16 sectors have been defined. The drawn contours can be copied to other images for the same slice position in the perfusion study. After adjustment of the contours in each image, the software calculated the mean signal intensity in each myocardial sector. As a result, one can obtain graphs depicting the change in signal intensity in each myocardial sector as a function of image number or time (see *inset panel*)

in the data set, or an automated algorithm is employed to identify the borders of the myocardium and this self-adjusts the contour positions. The latter approach is extremely useful (or even essential), as the number of images in a perfusion data set can be very large compared to a cine data set. In other words, the task of simply copying the contours to all other images would require extensive manual editing of the contour by the user. Unlike cine images, the myocardial boundaries can be slightly blurred in perfusion images due to the reduced spatial resolution and cardiac motion. Segmentation of myocardial perfusion images is therefore considered typically more challenging than for cine MR studies.

Once the myocardium is extracted by image segmentation, it is divided into smaller segments or sectors similar to those defined in cine wall motion analyses and corresponding to the individual coronary supplied territories [118]. The signal intensity averages can be plotted versus the image number or versus the time from the beginning of the perfusion scan. Various parameters that will characterize the contrast enhancement kinetics are computed from these signal intensity curves for assessing perfusion (see below). A typical interface with the software tool that can be used for analysis of MR perfusion studies is shown in Fig. 24.17.

As the perfusion images are acquired quite rapidly (<250 ms per image), there is often significant noise in the embedded images. Thus, to extract perfusion parameters, it is useful to perform some curve fitting, to smooth out these signal intensity curves. One widely used method for this purpose is the gamma variate function [119] which approximates the first pass portion of the measured curves quite well. A gamma variate curve fitted to a signal intensity curve obtained from an MR perfusion study in a patient study is

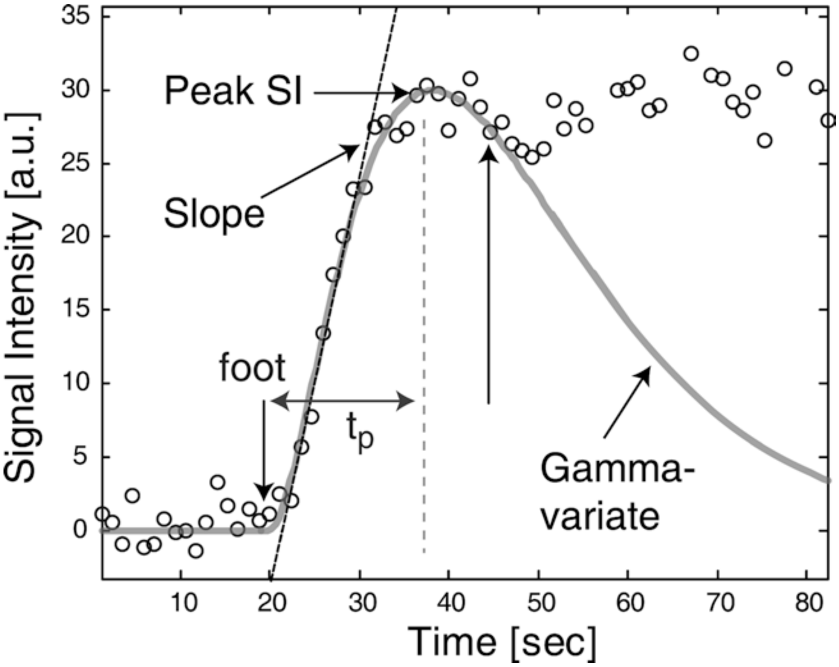

Fig. 24.18 Signal intensity curve for a myocardial sector in the lateral wall. Each of the data points (*round circles*) represents the mean signal intensity measured in the images for the user-defined myocardial sector. The images were acquired with a fast T_1-weighted gradient echo sequence during injection of a 0.075 mmol/kg bolus of Gd-DTPA, an extracellular MR contrast agent. The gamma variate function can only be used to fit the portion of the tissue curve corresponding to the first pass of the contrast agent. The *gray curve* represents the best fit of gamma variate function to be part of the experimental data, covering the range indicated by the *vertical arrows*. The gamma variate fit was extrapolated to the end of the measurement range. In many cases, the end of the first pass and the appearance of the recirculation component can be best ascertained from the signal intensity changes observed in the left ventricular blood pool. Also shown are semi-quantitative perfusion parameters such as the slope, peak signal intensity, and the time from the foot to the peak (t_p)

shown in Fig. 24.18. Nevertheless, there are certain constraints for gamma variate analysis, e.g., it is best optimized only when the first pass portion of the curve is used (from the foot to the peak of the curve).

To date, a number of parameters have been proposed for a semi-quantitative assessment of perfusion. Commonly used parameters are:

- *Percent peak enhancement*: The peak signal normalized by the derived average baseline signal, i.e., signal before arrival of contrast agent expressed as a percentage.
- *Upslope*: The slope of the first pass segment primarily from the start of appearance of the contrast (foot) in the myocardium to the peak.
- *Time to peak*: The time from the foot to the peak of the curve.
- *Mean transit time*: The average time required for a unit volume of blood to transit through the region of interest. It can be determined as the ratio of blood volume in the region of interest to the blood flow through the region of interest. This value can be estimated from the gamma variate fit to the tissue curve.
- *Dynamic distribution volume*: The area under the signal intensity curve, often normalized by the area under the corresponding curve for the left ventricle.

More recently, the upslope parameter has become the most widely used parameter for a semi-quantitative evaluation of myocardial perfusion. The upslopes of the tissue curves are generally normalized by the upslope of the signal intensity curve for a region of interest in the center of the left ventricle, with the latter being considered as an arterial input in such analyses. A ratio, defined as the normalized upslope of the tissue curve measured for maximal vasodilation, divided by the corresponding upslope value at rest, has been proposed as a perfusion reserve index [120–123]. Yet, the perfusion reserve derived from the upslopes generally underestimates the actual ratio of blood flow for maximal vasodilation and rest by approximately 40 % [124].

Our research group has shown that accurate myocardial blood flow estimates can be obtained by MRI methodologies, in comparison to invasive studies employing radio isotope labeled microspheres [125–128]; note that the latter are acknowledged as gold standards for the measurement of blood flow in tissues. MRI perfusion imaging may therefore play a pivotal future role in assessing novel therapeutic approaches for treating coronary artery disease, and automated quantitative analyses of MR perfusion measurements would play an essential role in this task.

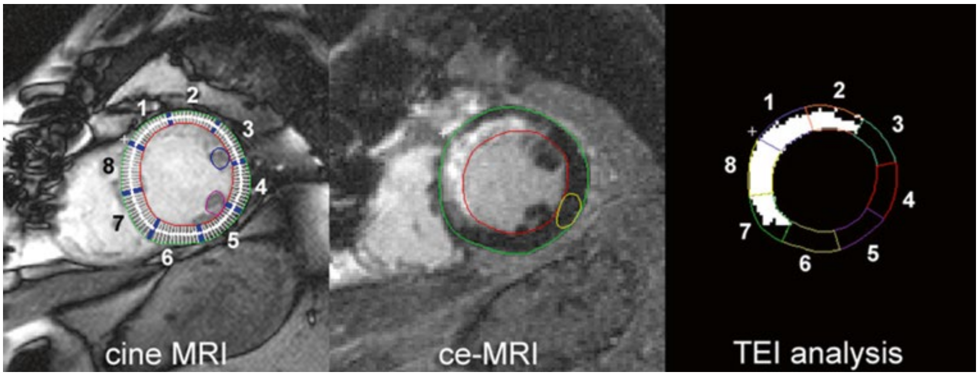

Fig. 24.19 Relative correspondence between the cine (*left*) image showing the 100 chords calculated using the center line method (grouped into eight segments per slice), contrast-enhanced MRI (ce-MRI) (*middle*) showing hyperenhanced scar region with the transmural extent of infarction (*TEI*) calculated in the eight segments (*right*)

24.5.4 Myocardial Scar Size

Myocardial infarct scar sizing and the identification of dysfunctional but potentially viable myocardium are the major prognostic indicators for the recovery of function after a myocardial infarction and have important clinical implications [129–132]. As such, myocardial infarct sizes measured using delayed ce-MRI has been shown to correlate well with histological measurements in both acute and chronic settings [35, 133]. Furthermore, ce-MRI offers distinct advantages over other imaging modalities that either rely on the functional recovery of wall motion abnormalities to identify viability [17] or which are not able to accurately depict smaller subendocardial infarctions [40]. Because of these advantages, ce-MRI is increasingly being used to quantify scar sizes in the acute and chronic setting and to predict the recovery of regional myocardial function using measurements of the segmental “transmural extent of infarction” (TEI) [37, 38, 134, 135]. Importantly, the exact measurement of given infarct size with ce-MRI is of particular interest because both early revascularization and lytic therapy have been shown to lead to a reduced incidence of transmural infarctions, and also myocardial infarcts tend to be patchy [136, 137].

For the ce-MRI images, pixels containing nonviable myocardium have signal intensities statistically greater (hyperenhanced) than a baseline sample from a remote normal region. Typically, hyperenhanced pixels have been classified as those with signal intensities greater than the mean ± standard deviations of a remote normal region [138, 139]. This threshold, whether manually or statistically defined, is highly subjective and highly dependent on the image quality and the noise present. Regions of signal hypoenhancement, associated with microvascular obstruction [33, 134] in the acute infarct case are typically manually segmented and included as scar. The TEI can also be computed for each segment as the ratio (%) of scar to nonscar pixels (Fig. 24.19). Overall scar size is computed by summing the myocardial scar volume in each slice throughout the heart. Finally, infarct extent can be calculated as the scar volume divided by the myocardial volume.

24.6 Summary

For the biomedical engineer, cardiac MRI represents an opportunity to study the function of the heart and use these insights to design better biomedical devices. Due to the increasing relevance of cardiac MRI in the clinical arena, it will become even more important to address the challenges inherent in the use of cardiac MRI in patients with implanted devices, although recent advancements have been made. It should be noted that numerous topics such as MR coronary angiography and plaque imaging, although of great interest, have been left out of this overview of cardiac MRI.

References

1. Pettigrew RI (1989) Dynamic cardiac MR imaging. Techniques and applications. Radiol Clin North Am 27:1183–1203
2. Bloomgarden DC et al (1997) Global cardiac function using fast breath-hold MRI: validation of new acquisition and analysis techniques. Magn Reson Med 37:683–692
3. Sakuma H et al (1993) Evaluation of left ventricular volume and mass with breath-hold cine MR imaging. Radiology 188:377–380
4. Anand IS et al (2002) Noninvasive assessment of left ventricular remodeling: concepts, techniques, and implications for clinical trials. J Card Fail 8(6 Suppl):S452–S464
5. Atkinson DJ, Edelman RR (1991) Cineangiography of the heart in a single breath hold with a segmented turboFLASH sequence. Radiology 178:357–360
6. Bluemke DA et al (1997) Segmented K-space cine breath-hold cardiovascular MR imaging: Part 1. Principles and technique. AJR Am J Roentgenol 169:395–400
7. Bluemke DA et al (1997) Segmented K-space cine breath-hold cardiovascular MR imaging: Part 2. Evaluation of aortic vasculopathy. AJR Am J Roentgenol 169:401–407
8. Chien D, Edelman RR (1991) Ultrafast imaging using gradient echoes. Magn Reson Q 7:31–56
9. Oppelt A et al (1986) FISP: a new fast MRI sequence. Electromedica 54:15–18
10. Zur Y, Wood ML, Neuringer LJ (1990) Motion-insensitive, steady-state free precession imaging. Magn Reson Med 16:444–459
11. Pereles FS et al (2001) Usefulness of segmented trueFISP cardiac pulse sequence in evaluation of congenital and acquired adult cardiac abnormalities. AJR Am J Roentgenol 177:1155–1160

12. Plein S et al (2001) Steady-state free precession magnetic resonance imaging of the heart: comparison with segmented k-space gradient-echo imaging. J Magn Reson Imaging 14:230–236
13. Francois CJ et al (2004) Left ventricular mass: manual and automatic segmentation of true FISP and FLASH cine MR images in dogs and pigs. Radiology 230:389–395
14. Shors SM et al (2004) Accurate quantification of right ventricular mass at MR imaging by using cine true fast imaging with steady-state precession: study in dogs. Radiology 230:383–388
15. Yang X et al (2001) Magnetic resonance imaging permits in vivo monitoring of catheter-based vascular gene delivery. Circulation 104:1588–1590
16. Weiger M, Pruessmann KP, Boesiger P (2000) Cardiac real-time imaging using SENSE. SENSitivity Encoding scheme. Magn Reson Med 43:177–184
17. Penicka M et al (2004) Tissue Doppler imaging predicts recovery of left ventricular function after recanalization of an occluded coronary artery. J Am Coll Cardiol 43:85–91
18. Sanz G et al (1982) Determinants of prognosis in survivors of myocardial infarction: a prospective clinical angiographic study. N Engl J Med 306:1065–1070
19. Weiss JL, Marino PN, Shapiro EP (1991) Myocardial infarct expansion: recognition, significance and pathology. Am J Cardiol 68:35D–40D
20. Lieberman AN et al (1981) Two-dimensional echocardiography and infarct size: relationship of regional wall motion and thickening to the extent of myocardial infarction in the dog. Circulation 63:739–746
21. Sasayama S et al (1976) Dynamic changes in left ventricular wall thickness and their use in analyzing cardiac function in the conscious dog. Am J Cardiol 38:870–879
22. Azhari H et al (1995) A noninvasive comparative study of myocardial strains in ischemic canine hearts using tagged MRI in 3-D. Am J Physiol 268:H1918–H1926
23. Gotte MJ et al (2001) Quantification of regional contractile function after infarction: strain analysis superior to wall thickening analysis in discriminating infarct from remote myocardium. J Am Coll Cardiol 37:808–817
24. Rickers C et al (2004) Applications of magnetic resonance imaging for cardiac stem cell therapy. J Interv Cardiol 17:37–46
25. Axel L, Goncalves RC, Bloomgarden D (1992) Regional heart wall motion: two-dimensional analysis and functional imaging with MR imaging. Radiology 183:745–750
26. Clark NR et al (1991) Circumferential myocardial shortening in the normal human left ventricle. Assessment by magnetic resonance imaging using spatial modulation of magnetization. Circulation 84:67–74
27. McVeigh ER (1996) MRI of myocardial function: motion tracking techniques. Magn Reson Imaging 14:137–150
28. McVeigh ER, Atalar E (1992) Cardiac tagging with breath-hold cine MRI. Magn Reson Med 28:318–327
29. McVeigh ER, Zerhouni EA (1991) Noninvasive measurement of transmural gradients in myocardial strain with MR imaging. Radiology 180:677–683
30. Koenig SH et al (1986) Relaxation of water protons in the intra- and extracellular regions of blood containing Gd(DTPA). Magn Reson Med 3:791–795
31. Strich G et al (1985) Tissue distribution and magnetic resonance spin lattice relaxation effects of gadolinium-DTPA. Radiology 154:723–726
32. Braunwald E (ed) (1997) Heart disease: a textbook of cardiovascular medicine. W.B. Saunders Company, Philadelphia
33. Lima JA et al (1995) Regional heterogeneity of human myocardial infarcts demonstrated by contrast-enhanced MRI. Potential mechanisms. Circulation 92:1117–1125
34. Tsekos NV et al (1995) Fast anatomical imaging of the heart and assessment of myocardial perfusion with arrhythmia insensitive magnetization preparation. Magn Reson Med 34:530–536
35. Kim RJ et al (1999) Relationship of MRI delayed contrast enhancement to irreversible injury, infarct age, and contractile function. Circulation 100:1992–2002
36. Simonetti OP et al (2001) An improved MR imaging technique for the visualization of myocardial infarction. Radiology 218:215–223
37. Bello D et al (2003) Gadolinium cardiovascular magnetic resonance predicts reversible myocardial dysfunction and remodeling in patients with heart failure undergoing beta-blocker therapy. Circulation 108:1945–1953
38. Kim RJ et al (2000) The use of contrast-enhanced magnetic resonance imaging to identify reversible myocardial dysfunction. N Engl J Med 343:1445–1453
39. Klein C et al (2002) Assessment of myocardial viability with contrast-enhanced magnetic resonance imaging: comparison with positron emission tomography. Circulation 105:162–167
40. Wagner A et al (2003) Contrast-enhanced MRI and routine single photon emission computed tomography (SPECT) perfusion imaging for detection of subendocardial myocardial infarcts: an imaging study. Lancet 361:374–379
41. Lekx KS et al (2004) The partition coefficient of Gd-DTPA reflects maintained tissue viability in a canine model of chronic significant coronary stenosis. J Cardiovasc Magn Reson 6:33–42
42. Tong CY et al (1993) Measurement of the extraction efficiency and distribution volume for Gd-DTPA in normal and diseased canine myocardium. Magn Reson Med 30:337–346
43. Wendland MF et al (2002) Thallium-like test for myocardial viability with MnDPDP-enhanced MRI. Acad Radiol 9(Suppl 1):S82–S83
44. Kim RJ et al (1999) Relationship of elevated 23Na magnetic resonance image intensity to infarct size after acute reperfused myocardial infarction. Circulation 100:185–192
45. Duprez DA et al (2007) Heterogeneous remodelling of the ascending and descending aorta with age. J Hum Hypertens 21:689–691
46. Hsu EW et al (1998) Magnetic resonance myocardial fiber-orientation mapping with direct histological correlation. Am J Physiol 274:H1627–H1634
47. LeGrice IJ et al (1995) Laminar structure of the heart: ventricular myocyte arrangement and connective tissue architecture in the dog. Am J Physiol 269:H571–H582
48. Streeter DD Jr et al (1969) Fiber orientation in the canine left ventricle during diastole and systole. Circ Res 24:339–347
49. Ingels NB Jr (1997) Myocardial fiber architecture and left ventricular function. Technol Health Care 5:45–52
50. Rijcken J et al (1997) Optimization of cardiac fiber orientation for homogeneous fiber strain at beginning of ejection. J Biomech 30:1041–1049
51. Rijcken J et al (1999) Optimization of cardiac fiber orientation for homogeneous fiber strain during ejection. Ann Biomed Eng 27:289–297
52. Sallin EA (1969) Fiber orientation and ejection fraction in the human left ventricle. Biophys J 9:954–964
53. Tomioka H et al (2006) The effect of ventricular sequential contraction on helical heart during pacing: high septal pacing versus biventricular pacing. Eur J Cardiothorac Surg 29(Supp 1):S198–S206
54. Tseng WY et al (2000) Myocardial fiber shortening in humans: initial results of MR imaging. Radiology 216:128–139
55. Van Der Toorn A et al (2002) Transmural gradients of cardiac myofiber shortening in aortic valve stenosis patients using MRI tagging. Am J Physiol Heart Circ Physiol 283:H1609–H1615
56. Shapiro EP, Rademakers FE (1997) Importance of oblique fiber orientation for left ventricular wall deformation. Technol Health Care 5:21–28

57. Tseng WY et al (2003) Diffusion tensor MRI of myocardial fibers and sheets: correspondence with visible cut-face texture. J Magn Reson Imaging 17:31–42
58. Helm PA et al (2005) Ex vivo 3D diffusion tensor imaging and quantification of cardiac laminar structure. Magn Reson Med 54:850–859
59. Scollan DF et al (2000) Reconstruction of cardiac ventricular geometry and fiber orientation using magnetic resonance imaging. Ann Biomed Eng 28:934–944
60. Geerts L et al (2002) Characterization of the normal cardiac myofiber field in goat measured with MR-diffusion tensor imaging. Am J Physiol Heart Circ Physiol 283:H139–H145
61. Basser PJ, Mattiello J, LeBihan D (1994) Estimation of the effective self-diffusion tensor from the NMR spin echo. J Magn Reson B 103:247–254
62. Garrido L et al (1994) Anisotropy of water diffusion in the myocardium of the rat. Circ Res 74:789–793
63. Holmes AA, Scollan DF, Winslow RL (2000) Direct histological validation of diffusion tensor MRI in formaldehyde-fixed myocardium. Magn Reson Med 44:157–161
64. Scollan DF et al (1998) Histological validation of myocardial microstructure obtained from diffusion tensor magnetic resonance imaging. Am J Physiol 275:H2308–H2318
65. Helm P et al (2005) Measuring and mapping cardiac fiber and laminar architecture using diffusion tensor MR imaging. Ann N Y Acad Sci 1047:296–307
66. Dou J et al (2003) Combined diffusion and strain MRI reveals structure and function of human myocardial laminar sheets in vivo. Magn Reson Med 50:107–113
67. Reese TG et al (1995) Imaging myocardial fiber architecture in vivo with magnetic resonance. Magn Reson Med 34:786–791
68. Rohmer D, Sitek A, Gullberg GT (2007) Reconstruction and visualization of fiber and laminar structure in the normal human heart from ex vivo diffusion tensor magnetic resonance imaging (DTMRI) data. Invest Radiol 42:777–789
69. Eggen MD, Swingen CM, Iaizzo PA (2012) Ex vivo diffusion tensor MRI of human hearts: relative effects of specimen decomposition. Magn Reson Med 67:1703–1709
70. Tseng WY et al (2006) Imaging myocardial fiber disarray and intramural strain hypokinesis in hypertrophic cardiomyopathy with MRI. J Magn Reson Imaging 23:1–8
71. Chen J et al (2003) Remodeling of cardiac fiber structure after infarction in rats quantified with diffusion tensor MRI. Am J Physiol Heart Circ Physiol 285:H946–H954
72. Wu MT et al (2006) Diffusion tensor magnetic resonance imaging mapping the fiber architecture remodeling in human myocardium after infarction: correlation with viability and wall motion. Circulation 114:1036–1045
73. Vadakkumpadan F et al (2010) Image-based models of cardiac structure in health and disease. Wiley Interdiscip Rev Syst Biol Med 2:489–506
74. Arevalo H et al (2013) Tachycardia in post-infarction hearts: insights from 3D image-based ventricular models. PLoS One 8, e68872
75. Lardo AC (2000) Real-time magnetic resonance imaging: diagnostic and interventional applications. Pediatr Cardiol 21:80–98
76. Kerr AB et al (1997) Real-time interactive MRI on a conventional scanner. Magn Reson Med 38:355–367
77. Serfaty JM et al (2003) MRI-guided coronary catheterization and PTCA: a feasibility study on a dog model. Magn Reson Med 49:258–263
78. Lardo AC et al (2000) Visualization and temporal/spatial characterization of cardiac radiofrequency ablation lesions using magnetic resonance imaging. Circulation 102:698–705
79. Atalar E et al (1996) High resolution intravascular MRI and MRS by using a catheter receiver coil. Magn Reson Med 36:596–605
80. Moore P (2005) MRI-guided congenital cardiac catheterization and intervention: the future? Catheter Cardiovasc Interv 66:1–8
81. Gaspar T et al (2014) Three-dimensional real-time MRI-guided intracardiac catheter navigation. Eur Heart J 35:589
82. Bell JA et al (2012) A deflectable guiding catheter for real-time MRI-guided interventions. J Magn Reson Imaging 35:908–915
83. McVeigh ER et al (2006) Real-time interactive MRI-guided cardiac surgery: aortic valve replacement using a direct apical approach. Magn Reson Med 56:958–964
84. Kahlert P et al (2012) Towards real-time cardiovascular magnetic resonance guided transarterial CoreValve implantation: in vivo evaluation in swine. J Cardiovasc Magn Reson 14:21
85. Saikus CE, Lederman RJ (2009) Interventional cardiovascular magnetic resonance imaging: a new opportunity for image-guided interventions. JACC Cardiovasc Imaging 2:1321–1331
86. Eitel C et al (2014) Catheter ablation guided by real-time MRI. Curr Cardiol Rep 16:511
87. Saeed M et al (2012) MR fluoroscopy in vascular and cardiac interventions (review). Int J Cardiovasc Imaging 28:117–137
88. ASTM F2503-13 (2013) Standard practice for marking medical devices and other items for safety in the magnetic resonance environment. ASTM International, West Conshohocken, PA
89. Cronin EM, Mahon N, Wilkoff BL (2012) MRI in patients with cardiac implantable electronic devices. Expert Rev Med Devices 9:139–146
90. Wilkoff BL et al (2011) Magnetic resonance imaging in patients with a pacemaker system designed for the magnetic resonance environment. Heart Rhythm 8:65–73
91. Wilkoff BL et al (2013) Safe magnetic resonance imaging scanning of patients with cardiac rhythm devices: a role for computer modeling. Heart Rhythm 10:1815–1821
92. Schwitter J et al (2013) Impact of the Advisa MRI pacing system on the diagnostic quality of cardiac MR images and contraction patterns of cardiac muscle during scans: Advisa MRI randomized clinical multicenter study results. Heart Rhythm 10:864–872
93. Stevens SM et al (2014) Device artifact reduction for magnetic resonance imaging of patients with implantable cardioverter-defibrillators and ventricular tachycardia: late gadolinium enhancement correlation with electroanatomic mapping. Heart Rhythm 11:289–298
94. Nitz WR et al (2001) On the heating of linear conductive structures as guide wires and catheters in interventional MRI. J Magn Reson Imaging 13:105–114
95. Yeung CJ, Susil RC, Atalar E (2002) RF safety of wires in interventional MRI: using a safety index. Magn Reson Med 47:187–193
96. Houlind K et al (1996) Magnetic resonance imaging of blood velocity distribution around St. Jude medical aortic valves in patients. J Heart Valve Dis 5:511–517
97. Walker PG et al (1995) Magnetic resonance velocity imaging: a new method for prosthetic heart valve study. J Heart Valve Dis 4:296–307
98. Botnar R et al (2000) Assessment of prosthetic aortic valve performance by magnetic resonance velocity imaging. MAGMA 10:18–26
99. Wyman BT et al (2002) Effects of single- and biventricular pacing on temporal and spatial dynamics of ventricular contraction. Am J Physiol Heart Circ Physiol 282:H372–H379
100. Eggen MD et al (2010) MRI assessment of pacing induced ventricular dyssynchrony in an isolated human heart. J Magn Reson Imaging 31:466–469
101. van der Geest RJ et al (1997) Quantitative analysis of cardiovascular MR images. Int J Card Imaging 13:247–258
102. van der Geest RJ, Lelieveldt BP, Reiber JH (2000) Quantification of global and regional ventricular function in cardiac magnetic resonance imaging. Top Magn Reson Imaging 11:348–358

103. van der Geest RJ, Reiber JH (1999) Quantification in cardiac MRI. J Magn Reson Imaging 10:602–608
104. Young AA et al (2000) Left ventricular mass and volume: fast calculation with guide-point modeling on MR images. Radiology 216:597–602
105. Swingen CM, Seethamraju RT, Jerosch-Herold M (2003) Feedback-assisted three-dimensional reconstruction of the left ventricle with MRI. J Magn Reson Imaging 17:528–537
106. Swingen C, Wang X, Jerosch-Herold M (2004) Evaluation of myocardial volume heterogeneity during end-diastole and end-systole using cine MRI. J Cardiovasc Magn Reson 6:829–835
107. Baer FM et al (1995) Comparison of low-dose dobutamine-gradient-echo magnetic resonance imaging and positron emission tomography with [18F]fluorodeoxyglucose in patients with chronic coronary artery disease. A functional and morphological approach to the detection of residual myocardial viability. Circulation 91:1006–1015
108. Baer FM et al (1996) Comparison of dobutamine transesophageal echocardiography and dobutamine magnetic resonance imaging for detection of residual myocardial viability. Am J Cardiol 78:415–419
109. Nagel E et al (1999) Noninvasive diagnosis of ischemia-induced wall motion abnormalities with the use of high-dose dobutamine stress MRI: comparison with dobutamine stress echocardiography. Circulation 99:763–770
110. Matheijssen NA et al (1993) Left ventricular wall motion analysis in patients with acute myocardial infarction using magnetic resonance imaging. Magn Reson Imaging 11:485–492
111. Holman ER et al (1995) Quantitative analysis of regional left ventricular function after myocardial infarction in the pig assessed with cine magnetic resonance imaging. Magn Reson Med 34:161–169
112. Nagel E, Fleck E (1999) Functional MRI in ischemic heart disease based on detection of contraction abnormalities. J Magn Reson Imaging 10:411–417
113. Sheehan FH et al (1986) Advantages and applications of the centerline method for characterizing regional ventricular function. Circulation 74:293–305
114. Osman NF et al (1999) Cardiac motion tracking using CINE harmonic phase (HARP) magnetic resonance imaging. Magn Reson Med 42:1048–1060
115. Osman NF, McVeigh ER, Prince JL (2000) Imaging heart motion using harmonic phase MRI. IEEE Trans Med Imaging 19:186–202
116. Osman NF, Prince JL (2000) Visualizing myocardial function using HARP MRI. Phys Med Biol 45:1665–1682
117. Kraitchman D et al (2001) Detecting the onset of ischemia using real-time HARP. Proceedings of the International Society of Magnetic Resonance in Medicine
118. Cerqueira MD et al (2002) Standardized myocardial segmentation and nomenclature for tomographic imaging of the heart: a statement for healthcare professionals from the Cardiac Imaging Committee of the Council on Clinical Cardiology of the American Heart Association. Circulation 105:539–542
119. Thompson HK Jr et al (1964) Indicator transit time considered as a gamma variate. Circ Res 14:502–515
120. Al-Saadi N et al (2000) Noninvasive detection of myocardial ischemia from perfusion reserve based on cardiovascular magnetic resonance. Circulation 101:1379–1383
121. Al-Saadi N et al (2000) Improvement of myocardial perfusion reserve early after coronary intervention: assessment with cardiac magnetic resonance imaging. J Am Coll Cardiol 36:1557–1564
122. Panting JR et al (2002) Abnormal subendocardial perfusion in cardiac syndrome X detected by cardiovascular magnetic resonance imaging. N Engl J Med 346:1948–1953
123. Schwitter J et al (2001) Assessment of myocardial perfusion in coronary artery disease by magnetic resonance: a comparison with positron emission tomography and coronary angiography. Circulation 103:2230–2235
124. Ibrahim T et al (2002) Assessment of coronary flow reserve: comparison between contrast-enhanced magnetic resonance imaging and positron emission tomography. J Am Coll Cardiol 39:864–870
125. Jerosch-Herold M et al (2003) Magnetic resonance imaging of myocardial contrast enhancement with MS-325 and its relation to myocardial blood flow and the perfusion reserve. J Magn Reson Imaging 18:544–545
126. Jerosch-Herold M et al (2004) Analysis of myocardial perfusion MRI. J Magn Reson Imaging 19:758–770
127. Jerosch-Herold M, Swingen C, Seethamraju RT (2002) Myocardial blood flow quantification with MRI by model-independent deconvolution. Med Phys 29:886–897
128. Jerosch-Herold M et al (1999) Direct comparison of an intravascular and an extracellular contrast agent for quantification of myocardial perfusion. Cardiac MRI Group. Int J Card Imaging 15:453–464
129. Baer FM et al (1999) MRI assessment of myocardial viability: comparison with other imaging techniques. Rays 24:96–108
130. Haas F et al (1997) Preoperative positron emission tomographic viability assessment and perioperative and postoperative risk in patients with advanced ischemic heart disease. J Am Coll Cardiol 30:1693–1700
131. Lee KS et al (1994) Prognosis of patients with left ventricular dysfunction, with and without viable myocardium after myocardial infarction. Relative efficacy of medical therapy and revascularization. Circulation 90:2687–2694
132. Pagley PR et al (1997) Improved outcome after coronary bypass surgery in patients with ischemic cardiomyopathy and residual myocardial viability. Circulation 96:793–800
133. Fieno DS et al (2000) Contrast-enhanced magnetic resonance imaging of myocardium at risk: distinction between reversible and irreversible injury throughout infarct healing. J Am Coll Cardiol 36:1985–1991
134. Beek AM et al (2003) Delayed contrast-enhanced magnetic resonance imaging for the prediction of regional functional improvement after acute myocardial infarction. J Am Coll Cardiol 42:895–901
135. Mahrholdt H et al (2003) Relationship of contractile function to transmural extent of infarction in patients with chronic coronary artery disease. J Am Coll Cardiol 42:505–512
136. Marino P, Zanolla L, Zardini P (1989) Effect of streptokinase on left ventricular modeling and function after myocardial infarction: the GISSI (Gruppo Italiano per lo Studio della Streptochinasi nell'Infarto Miocardico) Trial. J Am Coll Cardiol 14:1149–1158
137. Sheehan FH et al (1988) Early recovery of left ventricular function after thrombolytic therapy for acute myocardial infarction: an important determinant of survival. J Am Coll Cardiol 12:289–300
138. Gerber BL et al (2002) Accuracy of contrast-enhanced magnetic resonance imaging in predicting improvement of regional myocardial function in patients after acute myocardial infarction. Circulation 106:1083–1089
139. Kolipaka A et al (2005) Segmentation of non-viable myocardium in delayed enhancement magnetic resonance images. Int J Cardiovasc Imaging 21:303–311